

**Project Title:** High Flux Microchannel Receiver Development with Adaptive Flow Control

**Project Period:** (e.g. 01/01/14 – 12/31/16)

**Submission Date:** (07/15/15)

**Recipient:** Oregon State University  
**Address:** 204 Rogers Hall, Oregon State University  
Corvallis OR, 97331

**Website (if available)** oregonstate.edu

**Award Number:** DE-EE0005801

**Project Team:** Oregon State University (OSU) and Pacific Northwest National Laboratory (PNNL)

**Principal Investigator:** Kevin Drost  
Associate Professor  
Phone: 541-713-1344  
Email: [kevin.drost@oregonstate.edu](mailto:kevin.drost@oregonstate.edu)

**Business Contact:** Patricia Hawk - Director, Sponsored Programs  
Phone: 541-737-6699  
Email: [Patricia.Hawk@oregonstate.edu](mailto:Patricia.Hawk@oregonstate.edu)

**HQ Tech Manager:** Mark Lausten

**HQ Project Officer:** Thomas Rucker

**GO Grant Specialist:** Uriel Trujillo

**GO Contracting Officer:** Golden CO

**Executive Summary:** This project is focused on the demonstration of a microchannel-based solar receiver (MSR). The MSR concept consists of using a modular arrangement of arrayed microchannels to heat a working fluid in a concentrating solar receiver, allowing a much higher solar flux on the receiver and consequently a significant reduction in thermal losses, size, and cost. Others have shown that the ability to operate with a high incident flux is the key to improving receiver efficiency, allowing the use of high temperature heat transfer fluids, which in turn improve the energy conversion efficiency of the power block [1]. We are developing two design concepts, one using typical liquid heat transfer fluids such as molten salts and the second using gaseous heat transfer fluids such as supercritical CO<sub>2</sub> (sCO<sub>2</sub>). In each case the objective of the project is a laboratory demonstration of the technology that if successful will move the technology to a TRL 3.

Two MSR concepts have been developed: one for molten salt where the test article has the ability to absorb an average heat flux of 400 W/cm<sup>2</sup> with the exit temperature of the solar salt limited to 550°C and one for sCO<sub>2</sub> where the test article can an average flux of 100 W/cm<sup>2</sup> with sCO<sub>2</sub> exiting at 650°C

Experimental and simulation results have confirmed that the sCO<sub>2</sub> design can absorb 100 W/cm<sup>2</sup> of incident flux and have a receiver efficiency greater than 90% while heating sCO<sub>2</sub> to 650°C. The allowable incident flux is a factor of three or four higher than any previously reported for a gaseous heat transfer fluid.

Simulation has confirmed that our molten salt design can absorb 400 W/cm<sup>2</sup> of incident flux and have a receiver efficiency greater than 94%. Experiments have confirmed our ability to operate up to 150 W/cm<sup>2</sup> and, after addressing several equipment failures in our test apparatus, we are hoping to have experimental data confirming the ability to absorb 400 W/cm<sup>2</sup> in several weeks.

As part of the project we have identified materials and fabrication techniques that have allowed us to design, fabricate, and test microchannel devices capable of operating at 650°C with internal pressure of 80 to 200 bars. A preliminary design of a 100 MW<sub>e</sub> commercial scale receiver has been completed, and we have assessed the availability of high absorptivity coatings for these applications and concluded that attractive options are available.

## **Table of Contents**

1.0	Background .....	3
1.1	Microchannel Technology .....	3
1.2	Solar Receivers Relevant to Microchannel Development .....	4
2.0	Introduction .....	5
2.1	Microchannel Solar Receiver Concept .....	5
2.2	Significance, Innovations, and Fundamental Advances .....	7
2.3	Project Approach.....	8
3.0	Project Results and Discussion.....	12
3.1	Task 1- Microchannel Receiver Design and Simulation .....	12
3.2	Task 2 and 4- Test Article Fabrication.....	16
3.3	Task 3- Phase 1 Separate Effects Testing .....	21
3.4	Task 5- Phase 2 Separate Effects Testing .....	25
3.5	Tack 6- Integrated Test Article Design and Fabrication .....	32

3.6	Task 7- Optical Coating Selection .....	34
3.7	Task 8- Commercial Receiver Design .....	38
4.0	Conclusions .....	41
5.0	Budget and Schedule .....	43
6.0	Path Forward.....	44
7.0	References.....	44

**1.0 BACKGROUND:** The focus of this project is on the application of microchannel technology to concentrating solar power applications. This section will present a discussion of two technology areas: microchannel technology and solar receiver technology.

**1.1. Microchannel Technology:** In any diffusion-limited process, such as heat transfer, the residence time required for a fluid to come into equilibrium with the walls of a channel decreases as the square of the diffusion increases. Generally, the size of a heat transfer device is directly related to the residence time of the fluid being heated; hence, the size and cost of a device will decrease as the square of the diffusion length. This insight has led to the use of microchannels in a range of high flux heat transfer applications. The research herein described takes advantage of the extremely high heat transfer rates afforded by microchannels to demonstrate a microchannel-based solar receiver concept capable of absorbing high solar flux while using a variety of liquid and gaseous working fluids. The development of a high flux microchannel receiver has the potential to dramatically reduce the size and cost of a solar receiver by minimizing re-radiation and convective losses, thereby increasing the receiver efficiency. In this project, we have the objective of increasing incident flux by a factor of four for both a gas-like heat transfer fluid ( $sCO_2$ ) and a liquid (molten solar salt) while not significantly increasing the surface temperature of the receiver. This will result in a reduction in thermal losses by a factor of four. The microchannel solar receiver concept can be applied to a wide range of solar technologies, from dish concentrators to solar central receivers.

The ability of the microchannel solar receiver concept to reduce thermal losses is particularly important for high temperature applications. Given that re-radiation losses are a function of temperature to the fourth power, relatively small increases in the surface temperature of the receiver can result in a large increase in thermal losses. Figure 1 (following page) shows that higher concentration ratios (i.e., flux) increase both receiver efficiency and the optimum operating temperature of a solar thermal power plant, which in turn increases the efficiency of the power cycle. The red arrow in Fig. 1 represents the potential increase in efficiency at a receiver temperature of  $650^\circ C$  (923 K) by moving from a  $C=300$ , which is on the upper end of the current gaseous receivers, to  $C=1000$ , which is the goal with microchannel receivers. The blue arrow represents the increase in efficiency in going from the current  $C=500$  for a molten salt receiver to a  $C=4000$ , which is the goal with microchannel receivers.

Our extensive review of literature on microchannel heat transfer was presented in our first continuation report and will not be repeated here.

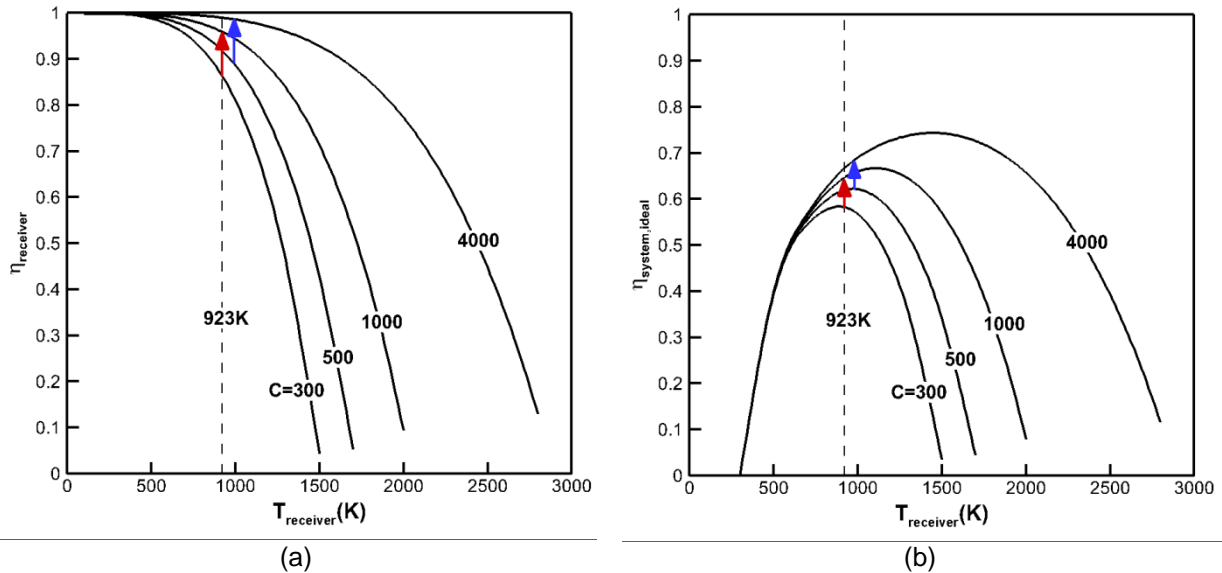


Figure 1. Idealized receiver efficiency (a) and solar thermal cycle efficiency (b) as a function of receiver operating temperature and concentration ratios [1].

**1.2 Solar Receivers Relevant to Microchannel Receiver Development:** Current solar central receivers operate at solar fluxes between 300 and 1000 kW/m<sup>2</sup>, or 30 to 100 W/cm<sup>2</sup> [3]. The status of advanced solar thermal central receiver technology was assessed by the U.S. Department of Energy (2012) [2], and two options for significantly improving the performance of solar thermal central receiver technology were identified: the use of high temperature molten salt, allowing the use of a supercritical Rankine power cycle and sCO<sub>2</sub> combined cycle power plant. The focus of this review is on the status of receiver technology necessary to realize these advanced power cycles.

The current status of molten salt technology, as represented by the Solar Two molten salt power plant was assessed by Pacheco 2002 [4]. In this case the receiver was producing 565°C molten salt and had a receiver efficiency of 88%, including absorptivity of 95% and an average flux of 43W/cm<sup>2</sup>. Kolb [5] evaluated the possibilities for the next generation high temperature molten salt power tower and estimated currently available receiver technology could operate with an incident flux on the order of 80 W/cm<sup>2</sup> [5]. Kolb estimated that with a development effort, this could be increased to 100 W/cm<sup>2</sup> with a corresponding thermal efficiency of 94% (or 89% total receiver efficiency, which includes reflection losses based on an absorptivity of 95%). Kolb, 2011, includes a particularly useful discussion of the impact of issues such as cyclic stresses and corrosion on receiver design. Kolb et al. [6] reviewed options for improving the performance and cost of molten salt receivers and indicated that future advanced molten salt receivers would need to achieve operating temperatures of 650°C and an incident flux of 100 W/cm<sup>2</sup> [6].

While a number of papers reviewing sCO<sub>2</sub> power cycles were identified, we found no references for the design or evaluation of a sCO<sub>2</sub> receiver. Based on published project summaries and presentations at Sunshot Annual Reviews, the Sunshot program is funding the development of alternative sCO<sub>2</sub> receivers by OSU and two other organizations. Brayton Energy has developed two designs. One operates at 750°C and will use a cavity and a low cost cover glass to reduce thermal losses [7]. A second open receiver

design was presented at the 2014 Sunshot Summit. Predicted receiver efficiency for this design or incident flux on the receiver surfaces was not reported. Based on presentations at the Sunshot Annual Review, NREL is also developing a sCO<sub>2</sub> receiver, but no information on the details of the design, incident flux, or performance was presented.

**2.0 INTRODUCTION:** In this section we provide a detailed description of the concept and relevance to SunShot goals, a discussion of technical feasibility and a summary of innovations and impact. Our primary objective is to significantly increase the allowable incident flux on a solar central receiver for a wide range of heat transfer fluids. Attaining a high flux in a receiver requires the solution of two problems. First, heat transfer must be sufficiently high to eliminate the need for a large temperature difference between the irradiated surface of the receiver and the heat transfer fluid. If the concept doesn't provide good heat transfer, the increased surface temperature of the receiver will increase reradiation and perhaps cause failure of the material. Secondly, an increase in flux requires an increase in the amount of heat transfer fluid flow per unit area of the receiver to remove the absorbed flux. An increase of allowable incident flux by a factor of four will increase the flow of heat transfer fluid per unit area of receiver by a factor of four. If nothing is done to address this issue, the pressure drop can be expected to increase by a factor of 16. The MSR addresses the first challenge with the use of small microchannels/micropins that reduce the diffusion barrier to heat transfer. The second challenge is addressed by using a geometry that allows the use of a large number of microchannels operating in parallel. A branching distribution system allows a large number of short microchannels to be used without an unreasonable pressure drop.

**2.1 Microchannel Solar Receiver Concept:** In any diffusion-limited process such as heat transfer, the residence time required for a fluid to come into equilibrium with the walls of a channel decreases as the square of the diffusion length increases. Over the last 25 years this phenomenon has been exploited in a large number of applications including heat exchangers, chemical reactors, mixers, and separations processes, and commercial microchannel devices are available from vendors such as Heatrix and Velocys. This research takes advantage of the extremely high heat transfer rates afforded by microchannels to demonstrate an MSR capable of absorbing high solar flux while using a variety of liquid and gaseous working fluids.

The MSR concept uses a modular arrangement of arrayed microchannels to heat a working fluid in a concentrating solar receiver. The modular array facilitates the branching fluidic distribution system that allows the use of many short parallel microchannels. An open solar central receiver would consist of an array of receiver panels in a roughly cylindrical arrangement. A 100-MW<sub>e</sub> receiver would require on the order of 250 1-m<sup>2</sup> panels arranged in a cylinder approximately 10 meters high and 8 meters in diameter (Figure 2). The receiver would include headers to provide heat transfer fluid to the modules and return hot fluid to the power block in addition to control valves or orifices to distribute flow to the modules. The receiver would also include structural

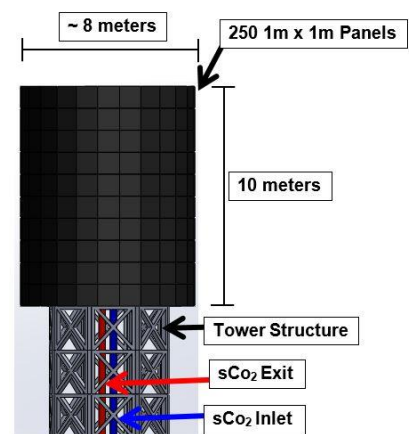


Figure 2. Representation of a 100-MW<sub>e</sub> open receiver.

supports where the modules would be attached. The design is inherently modular, with the large central receiver being assembled from identical 1-m<sup>2</sup> commercial panels. One key advantage of the modular design is the ability to independently vary the flow rates into the different receiver panels, ensuring a uniform exiting temperature of the heat transfer fluid.

The individual receiver panels will consist of a thin absorbing plate containing a large number of relatively short microchannels of channel dimensions on the order of hundreds of micrometers that absorbs the incident solar radiation with the aid of a high absorptivity coating. The microchannels are arranged into identical unit cells with a header system to distribute heat transfer fluid to each unit cell (Figure 3). The plate will be bonded to a second distribution plate with headers that distribute the working fluid to the unit cells, collect the heated working fluid and return it to a larger header for transport to the power block. An individual panel will be fabricated by using chemical etching or sinker Electric Discharge Machining (EDM) to form flow features into thin laminae of substrate material. The laminae will then be stacked and bonded to produce a thin receiver panel that includes the complex set of microchannels. While a number of bonding approaches exist, commercial production of microchannel receivers would most likely use diffusion bonding. Diffusion bonding is generally limited to 1-m<sup>2</sup> substrates, thus limiting the size of an individual module to approximately one 1 m<sup>2</sup>. A typical unit cell is shown in Figure 4. The unit cell consists of arrays of microscale pins located between an inlet and outlet header. Heat transfer fluid is distributed in the header and flows through the array of microscale pins where the fluid is heated. The hot fluid leaves the unit cell in the outlet header. As long as the pressure drop across the array of pins is ten times the pressure drop in the headers, the fluid will be evenly distributed through the pin array. The width of the pin array is fixed by the allowable pressure drop, which for sCO<sub>2</sub> is on the order of 3 to 4 cm. The length of the unit cell is fixed by pressure drop in the header that must be kept to 10% of the pressure drop in the pin array.

The MSR is an example of “numbering up” rather than scaling up. Numbering up involves the development of one standard module to conduct a unit operation where capacity is then increased by increasing the number of identical modules.

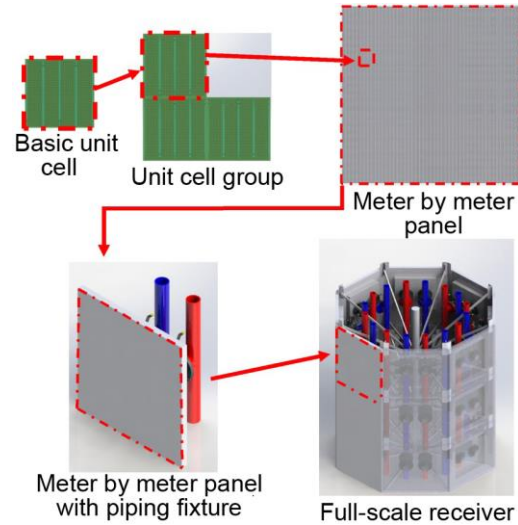


Figure 3. Illustration of 1 M<sup>2</sup> panel header concept showing distribution of flow from the global inlet and outlet to the individual 2-cm by 2-cm unit cells.

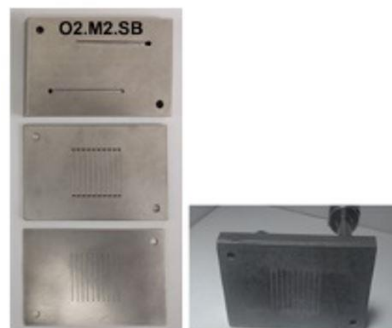


Fig. 4a. Microchannel unit cell. The microchannels cover an area of 2 cm x 2 cm with 1 inlet and 1 exit. The receiver is comprised of three plates.

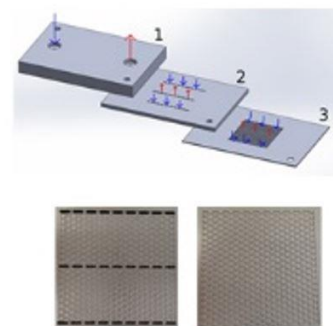


Figure 4b. Exploded view of the pin-fin unit cell showing the flux absorber plate (3), the middle flow distribution plate (2), and the upper header plate (1).

This is frequently done with laminated microchannel devices where the capacity of a unit operation is increased by adding more laminae. The advantage of numbering up is that it avoids the need for scaling up the process to larger capacity. In the case of the MSR, if we know the performance of one 1-m<sup>2</sup> module, we know the performance of a complete commercial-scale solar receiver because the performance of each module, as a function of incident flux, is identical.

## 2.2 Significance, Innovations, and Fundamental Advances:

**Innovations:** As discussed above, the MSR relies on two key innovations to attain high incident flux for both gaseous and liquid heat transfer fluids:

- **Use of microchannels to improve heat transfer**—The use of arrays of microscale pins for heat transfer is critical to reducing the temperature difference between the receiver surface and the heat transfer fluid. While OSU has applied microchannel architecture to dish concentrator solar natural gas reforming, to our knowledge the MSR is the first application of microchannels or microscale pin technology to central receiver power generation.
- **Use of a branching distribution system to allow a large number of short microchannels arranged in parallel**—A modular approach to the MSR is critical for maintaining a reasonable pressure drop in a high flux receiver application. The assembly of the full-scale receiver for commercial modules that has been assembled from unit cells allows a geometry with a very large number of short microscale flow paths operating in a parallel arrangement.

**Advantages and impact:** The primary advantages of the MSR technology are:

- **Improved receiver and plant efficiency**—Given that reradiation losses are a function of temperature to the fourth power, relatively small increases in the surface temperature of the receiver can result in a large increase in thermal losses. Higher concentration ratios (i.e., flux) increase both receiver efficiency and the optimum operating temperature of a solar thermal power plant, which in turn increase the efficiency of the power cycle. At a sCO<sub>2</sub> temperature of 650°C, increasing the flux from 30 W/cm<sup>2</sup> to 100 W/cm<sup>2</sup> increases the receiver efficiency from 86% to 96 % and the ideal system efficiency from 57% to 65%. Similarly, at a molten salt temperature of 600°C, increasing the flux from 100 W/cm<sup>2</sup> to 400 W/cm<sup>2</sup> increases the receiver efficiency from 90% to 98 % and the ideal system efficiency from 61% to 68% [1]
- **Applicable to a wide range of heat transfer fluids**—The MSR technology can be used with gases (sCO<sub>2</sub>, helium, etc.) or with liquids such as molten salt or liquid metal. Given the high pressure associated with sCO<sub>2</sub>, its use demonstrates a “worst case” scenario, and the successful development of the MSR for this application will result in the development of a technology also applicable to a range of other heat transfer fluids.
- **Reduced receiver size and cost**—The reduction in receiver size caused by high allowable incident flux will also reduce receiver cost and weight. When using expensive high temperature metals, the cost of the receiver will be a strong function of the amount of high temperature metal used in the device which is directly related to the size of the receiver. Preliminary production cost estimates for the commercial receiver module suggest that these can be produced at a cost of \$10,000 per module at production rates of 1,000 modules per year, which represents a cost of \$10/kW<sub>t</sub>. Field installation of the modules in to a

receiver will perhaps double or triple to cost to perhaps \$30/kWt, a small fraction of the Sunshot cost goal for the receiver.

As part of this project we have focused on the demonstration of two microchannel solar receiver concepts, one for liquid cooled microchannel receivers and one for gas cooling. Our performance objectives for each solar receiver concept are:

- **Liquid Working Fluid Metrics** - Our performance metric is to demonstrate, via results from the separate effects tests, that the 1cm-by-1cm molten salt receiver test article can achieve the targets of >95% thermal efficiency (where receiver efficiency is defined as the ratio of thermal energy transferred to the HTF divided by the solar flux incident on the receiver surface) with an HTF exit temperature of 565°C and pressure drop <2% of the inlet pressure while absorbing a heat flux of 400 W/cm<sup>2</sup>.
- **Gas Working Fluid Metrics** - Our metric for gaseous coolants is to demonstrate, via results from the separate effects tests, that the sCO<sub>2</sub> receiver targets of >90% thermal efficiency (where receiver efficiency is defined as the ratio of thermal energy transferred to the HTF divided by the solar flux incident on the receiver surface) with an HTF exit temperature of ≥650°C, a pressure drop of <0.35 bar while absorbing a heat flux of 100 W/cm<sup>2</sup> and to demonstrate computationally that pressure drop across inlet and outlet of a 1m<sup>2</sup> receiver panel is <2% of the inlet pressure and simultaneously achieving exit temperature of 650°C for a flux of 100 W/cm<sup>2</sup> for sCO<sub>2</sub>.

**2.3 Project Approach:** The proposed research is divided into three phases. Phase 1 lasted 12 months and was completed in August 2013. This phase focused on completing the design of the test articles and on the assembly of the test apparatus. Phase 2 started in September 2013 and lasted 12 months. Phase 2 focused on the experimental validation of our performance simulations and on performance testing of both sCO<sub>2</sub> and molten salt test articles. Phase 3 started in November 2014 and lasted eight months. Phase 3 focused on the assembly and pressure testing of a multi-unit cell test article and on the development of a conceptual design of a commercial scale receiver.

The approach to the project consisted of eight tasks. Task 1 was focused on the thermal/fluidic and mechanical simulation of the test articles; Task 2 involved the fabrication of test articles while Task 3 involved the fabrication of test articles for separate effects testing. Task 4 was the continuation of Task 3 in Phase 2 while Task 5 involved the actual separate effects testing of each of the test articles. Task 6 involved the design, fabrication, and pressure testing of an integrated test article with multiple unit cells and a distribution system. Optical coating suitable for sCO<sub>2</sub> applications were evaluated in Task 7, and a preconceptual design of a commercial receiver was included in Task 8. Each task is discussed below along with the related milestones. Our original scope of work included the demonstration of an adaptive flow control system and on-sun testing using a dish concentrator at the Pacific Northwest National Laboratory (PNNL). Following discussions with PNNL and the Sunshot program, these activities were not included in the project scope of work and will not be discussed further.

The project included three phases. Phase 1 involved the completion of Tasks 1, 2, and 3 while Phase 2 included the completion of Tasks 4 and 5. Tasks 6, 7 and 8 were completed as part of Phase 3. The Phase 1, 2 and 3 Go-No Go criteria are also presented below.

**Task 1 Microchannel Receiver Design and Simulation (T-1)**—In Task 1 we simulated key thermal processes including radiation heat transfer on the surface of the receiver, flow distribution through the array of microchannels, and heat transfer from the surface of the receiver to both the cooling fluid and ambient (reradiation and convection losses).

- **Milestone 1.1 (M1.1):** Based on simulation results OSU will have identified a design of a sCO<sub>2</sub> receiver operating at 650 °C capable of absorbing an average flux of 100 W/cm<sup>2</sup>. The pressure drop will be <0.35 bar and the surface temperature of the receiver will be consistent with a receiver thermal efficiency of 90% where receiver efficiency is defined as the ratio of thermal energy transferred to the heat transfer fluid (HTF) divided by the solar flux incident on the receiver surface.
- **Milestone 1.2 (M1.2):** Based on simulation results OSU will have identified a design of a solar salt microchannel receiver operating at a fluid exit temperature of 600°C capable of absorbing an average flux of 400 W/cm<sup>2</sup>. The pressure drop will be below 1.0 bar and the surface temperature of the receiver will be consistent with a receiver thermal efficiency of 95% where receiver efficiency.

**Task 2 Test Article Fabrication (T-2)**—Test articles were fabricated for both the separate effects tests and the integrated test using microlamination techniques (photo-chemical etching, sinker EDM, and diffusion bonding or laser welding). Corrosion, temperature compatibility, and manufacturability of candidate materials were reviewed, and OSU down selected materials for the sCO<sub>2</sub> separate effects test article, the sCO<sub>2</sub> integrated test article and the solar salt separate effects test article.

- **Milestone 2.1 (M2.1):** Deliver separate effects test article for sCO<sub>2</sub> that are leak-free at a sCO<sub>2</sub> pressure of 120 bars and can withstand the maximum surface temperature associated with a HTF exit temperature of 650 °C.

**Task 3 Separate Effects Testing (T-3)**—The goal of the separate effects test was to qualify the receiver over the range of heat fluxes. In addition to receiver characterization, separate effects testing allowed for validation of the numerical simulations performed in Task 1. During Phase 1 this task included the design, assembly, instrumentation, and calibration of the test facilities for sCO<sub>2</sub> and molten salt and the design, assembly, instrumentation, and calibration of high-flux solar simulator.

- **Milestone 3.1 (M3.1):** Complete assembly and calibration of the separate effects test facility and demonstrate that: 1) simulated solar source can deliver needed flux of 400 W/cm<sup>2</sup>; 2) the sCO<sub>2</sub> test facility is demonstrated to be leak free at operating temperature (650° C); and 3) the molten salt test facility is demonstrated to be leak free at an operating temperature of 565°C and all OSU safety requirements are met.

#### **Budget Period 1 Go/No Go Decision Point**

- **Go/No Go Decision (G/NG 1)**—Simulations have demonstrated microchannel receiver designs with <0.35 bar pressure drop for sCO<sub>2</sub> and <1 bar pressure drop for molten salt at operating temperature.
- **Go/No Go Decision (G/NG 2)**—Successful fabrication and testing of separate effects test articles capable of withstanding 120 bar pressure and the maximum surface temperature associated with a HTF exit temperature of temperature of 650°C

where the maximum surface temperature is taken from Task 1 simulation results.

- **Go/No GO Decision (G/NG 3)**—Successful demonstration of the solar simulator’s ability to produce 100 to 400 W/cm<sup>2</sup> solar flux and the successful pressure testing of the thermal test loops for sCO<sub>2</sub> and molten salt.

**Task 4 Test Article Fabrication (T-4)**—This task was the Phase 2 continuation of Task 2 and involved the fabrication of test articles for separate effects testing. Specifically this task included complete fabrication of the separate effects test articles that could withstand the maximum surface temperature associated with a HTF exit temperature of 650°C and 120 bar pressure and the complete fabrication of the molten salt separate effects test articles needed for the separate effects testing capable of withstanding 565°C operating temperature with test apparatus pressure of 2 bars.

- **Milestone 4.1 (M4.1)**: Deliver a separate effects test article (2-cm x 2-cm) that is leak free at the operating pressure of the separate effects test apparatus and can withstand operating temperatures of 650°C.
- **Milestone 4.2 (M4.2)**: Deliver a molten salt separate effects test article (1-cm x 1-cm) that is leak free and can withstand the maximum surface temperature associated with a heat transfer fluid exit temperature of 565°C.

**Task 5 Separate Effects Testing (T-5)**—The goal of the separate effects test was to qualify the receiver over the range of heat fluxes. In addition to receiver characterization, separate effects testing allowed for validation of the numerical simulations performed in Task 1 on global and local scales by measuring fluid temperatures, pressure drop, and receiver surface temperatures. This task included: 1) characterization of efficiency and receiver integrity in scaled separate effects experiments for an sCO<sub>2</sub> test article operating with an absorbed heat flux of 100 W/cm<sup>2</sup>; 2) characterization of efficiency and receiver integrity in scaled experiments for the molten salt receiver operating with an absorbed heat flux of 400 W/cm<sup>2</sup>; 3) characterization of the effects of scaling receiver on flow distribution, efficiency, and pressure drop and demonstration that a 2x increase in receiver size does not change the above targets; and 4) validation of the numerical simulations based on experimental results.

- **Milestone 5.1 (M5.1)**: Demonstrate, via results from the effects tests, that the sCO<sub>2</sub> receiver targets of >90% thermal efficiency while absorbing 100 W/cm<sup>2</sup> of solar flux and heating sCO<sub>2</sub> to 650°C.
- **Milestone 5.2 (M5.2)**: Demonstrate, via results from the effects tests, that the 1-cm by 1-cm molten salt receiver test article can achieve the targets of >95% thermal efficiency with an HTF exit temperature of 565°C while absorbing a heat flux of 400 W/cm.
- **Milestone 5.3 (M5.3)**: Demonstrate that receivers can be scaled by showing that the 2-cm by 2-cm receiver test article will have the same efficiency (heat flux of 100 W/cm<sup>2</sup> and pressure drop targets of 1 bar) as the smaller 1-cm by 2-cm test article.

#### **Budget Period 2 Go/No Go Decision Point**

- **Go/No Go Decision (G/NG 1)**—Deliver separate effects test article (2-cm x 2-cm) that is leak-free at the operating pressure of the integrated test and can withstand

operating temperatures of 650°C and 125 bars pressure.

- **Go/No Go Decision (G/NG 2)**—Demonstrate, via results from the separate effects tests, that the sCO<sub>2</sub> receiver targets of >90% thermal efficiency (where receiver efficiency is defined as the ratio of thermal energy transferred to the HTF divided by the solar flux incident on the receiver surface) with an HTF exit temperature of ≥650°C and a pressure drop less than 0.35 bar while absorbing a heat flux of 100 W/cm<sup>2</sup> are met.
- **Go/No Go Decision (G/NG 3)**—Demonstrate, via results from the effects tests, that the 1-cm by 1-cm molten salt receiver test article can achieve the targets of >95% thermal efficiency (where receiver efficiency is defined as the ratio of thermal energy transferred to the HTF divided by the solar flux incident on the receiver surface) with an HTF exit temperature of 565°C while absorbing a heat flux of 400 W/cm<sup>2</sup>.

**Task 6 Integrated Test Article Design and Fabrication (T-6)**—Integrated test articles were fabricated and the design was validated by pressure testing at temperature and tested for flow distribution using infrared imaging. This task included the fabrication of the leak free integrated test article (8 cm x 8 cm) able to withstand the maximum surface temperature associated with a HTF exit temperature of 650°C and designed for an operating pressure of 200 bars and flow testing of the 8 cm x 8 cm test article.

- **Milestone 6.1 (M6.1)**: Deliver a separate effects test article (8 cm x 8 cm) that is leak free at the operating pressure of the separate effects test apparatus and can withstand operating temperatures of 650°C and a pressure of at least 200 bars in accordance to ASME Section VIII Div. 1 codes.
- **Milestone 6.2 (M6.2)**: Use the solar simulator and infrared imaging to evaluate surface temperature that will be used to infer fluid flow distribution. Flow tests will be conducted to demonstrate pressure drop, flow distribution, and heat transfer match within 10% of that which is modeled when assuming even flow distribution to each unit cell. The total pressure drop from inlet to outlet header of the test article will be demonstrated to be less than an equivalent of 2% of inlet pressure when operating with sCO<sub>2</sub> pressure of 120 bars and a HTF exit temperature of 650°C.

**Task 7 Optical Coating Selection (T-7)**—The objective of this task was to evaluate high absorptivity optical coatings, validated by thermal testing in the solar simulator, and to select one for integration into the receiver design. A developer of optical coatings provided multiple coated test coupons. As a baseline reference, coupons were also coated with Pyromark using a suitable application method for Haynes substrate and for temperatures above 650°C. OSU measured adhesion using a tape test as well as the optical properties of all test coupons both before exposure to high temperature (650°C) and after several cycles of high temperature exposure.

- **Milestone 7.1 (M7.1)**: Identify a mechanically durable selective coating, targeting an absorptivity >95% after exposure to high temperature (650°C) in an air atmosphere.
- **Milestone 7.2 (M7.2)**: Complete thermal testing of the coated 2-cm by 2-cm test articles and validate that the inferred absorptivity of the test article is within 5% agreement of the measured coupon absorptivity.

**Task 8 Commercial Receiver Design (T-8)**—The objective of this task was to integrate the results from the three phases of the project to form a conceptual design for both a 1-m<sup>2</sup> MSR module and a complete commercial scale solar receiver base that could achieve receiver efficiency (reflection losses plus thermal losses) of 90%. Designs used the optical properties of the best performing optical coating identified in Task 7. The receiver was designed to heat sCO<sub>2</sub> to 650 °C at a pressure of 200 bars. The commercial receiver was sized to provide thermal energy to a 100 MWe power block.

- **Milestone 8.1 (M8.1):** Based on simulation results from subtask 8.1, the receiver designed to heat sCO<sub>2</sub> to 650 °C at a pressure of 200 bar achieves receiver efficiency (reflection losses plus thermal losses) of 90% and is sized to provide thermal energy to a 100 MWe power block. Absorbing surface optical properties will be based on the optical properties of the best performing optical coating identified in Task 7.

**3.0 PROJECT RESULTS AND DISCUSSION:** In this section, we will provide a summary of the work accomplished under each task described above.

**3.1 Task 1 - Microchannel Receiver Design and Simulation:** Simulations were used to develop designs for the molten salt and sCO<sub>2</sub> MSR test articles. The power requirements of our flux concentrator limited the size of the sCO<sub>2</sub> test article to a 2 cm by 2 cm absorbing surface when the flux generator was providing a simulated solar flux of 100 W/cm<sup>2</sup>. For similar reasons, the molten salt test article was limited to a 1 cm by 1 cm absorbing surface area when the flux generator was providing a simulated solar flux of 400 W/cm<sup>2</sup>. The approach for both molten salt and sCO<sub>2</sub> devices consisted of:

1. Establishing the general layout of the test article.
2. Using computational fluid dynamics simulation to predict flow distribution followed by design modifications to attain the desired uniformity of flow and pressure drop.
3. Using computational fluid dynamics simulation to solve the conjugate problem (combined conduction and convection in the test article) to predict temperature distribution and thermal efficiency.
4. Using the thermal results from 3 above to predict the mechanical and thermal stresses in the devices with a finite element simulation. The design was modified as needed to ensure that maximum stresses were acceptable for a test article.

The computational fluid and thermal analysis was carried out in three-dimensions using the commercial software Ansys. Most of the simulations involved complex configurations that combined Ansys' unstructured grid solver with grid generation software. In addition, Ansys provided coupling of the fluid solver with a conjugate heat transfer problem.

Fluid properties for supercritical carbon-dioxide were taken directly from Engineering Equation Solver (EES). The pressure in the device was held constant at the operating pressure of 120 bar because the change in pressure through the device is small. The temperature was varied from 700 to 1100°K. A polynomial curve-fit was computed for each fluid property of interest and used in the flow/thermal simulation.

For molten salt, fluid property data was extracted from plots on the Dynalene MS1 datasheet available on the company's website. Fluid properties were plotted as functions of temperature. However, for thermal conductivity, a constant value taken at 300°K

was reported. It is assumed that these data are taken at atmospheric pressure and that increasing the pressure to a range of 3 to 5 bar (operating pressure for molten salt device) will not have a significant impact on fluid properties. Polynomial curve fits were computed and used in Ansys Fluent.

For Haynes 230, the material selected for receiver fabrication, property data was extracted from plots on the datasheet available on the Haynes website. Properties were tabulated as functions of temperature, except for density, which is constant. A polynomial curve-fit was computed for each physical property of interest.

The thermal receiver efficiency is defined as the heat transferred to the fluid, or  $q''$ , divided by the heat absorbed on the receiver surface (not including reflection losses). Total receiver efficiency includes reflection losses from the receiver along with thermal losses. Total efficiency was calculated assuming a surface absorptivity of 0.95.

The finite element stress analysis was also conducted using Ansys. For stress analysis, mechanical properties for Haynes 230 were taken from the data sheet on the Haynes website. A constant value was used at an appropriate temperature, generally being the average temperature of the metal in the region being modeled. In order to evaluate stress analysis results and determine a factor of safety, creep strength was used. The benchmark used was 185 MPa, the 10-hour rupture strength at 790°C (1063°K). This temperature is based on the maximum temperature observed in the solid in the areas of highest stress for the various designs.

**3.1.1 sCO<sub>2</sub> Solar Receiver Test Article Designs**—After discussions with a number of vendors, we selected Haynes 230 as our material of fabrication and identified three options for completing the fabrication of the sCO<sub>2</sub> test article. These are discussed in section 3.2.

We will discuss the simulation results for Option 2 only, as Option 1 was a low risk design that would not be used in a commercial unit and the results for Option 2 were similar to Option 3.

Figures 5, 6, and 7 show isometric, inverted, and top wireframe views, respectively, of the final Option 2 design.

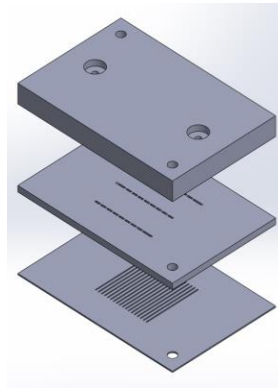


Figure 5. Isometric exploded view of option 2 design. Bottom-most plate is plate 1 and top-most plate is plate 3.

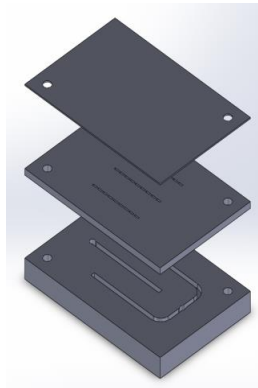


Figure 6. Top-most plate is plate 1 and bottom-most plate is plate 3.

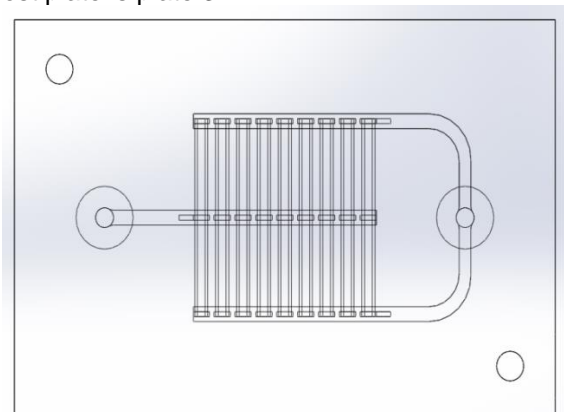


Figure 7. Top wireframe view of option 2 design. Fluid enters device through large hole on right. The inlet slot in plate 3 channels fluid to the entrance of the microchannels. Fluid in microchannels flows from top and bottom slots to the center slot and them out through the large hole on the left.

Fluid enters the device through the large circular hole on the right, splits between the two forks of the slot in plate 3, and enters the outer slots in plate 2. It then flows through the microchannels toward the middle slot, where it leaves plate 1, flows through the middle slot, enters the outlet slot in plate 3, and then exits the device.

Figure 8 shows a plot of mass flow rate versus channel position for the final option 2 design. Each data point represents an individual channel. There are 18 channels in total. The average pressure drop through the channels is 0.2 bar.

Figure 9 is a contour plot of temperature on the heated surface. The area seen is 1 cm by 2 cm (half of the total 2 cm by 2 cm area since symmetry was used). Fluid in the channels flows from top to bottom. The bottom edge is the symmetry boundary. The actual solid region modeled in this simulation extends beyond the area shown here; this is just the area to which the solar flux is applied. The average surface temperature is 980°K, and the receiver thermal efficiency is 94.7% (89.7% including reflection losses). Figure 10 is a contour plot of temperature of the solid at a cross-sectional plane at mid-length along the channels. Solar flux is incident to the bottom edge. Fluid in the channels flows into the page.

In the original header concept, each of the three headers (two inlet and one outlet) were a continuous slot with a uniform cross-section. The idea was to have the entire slot machined using wire EDM. This header featured two relatively large dimensions: the over 12-mm height and the 2-cm length that are necessary to deliver fluid to all of the channels that cover a 2-cm by 2-cm heated

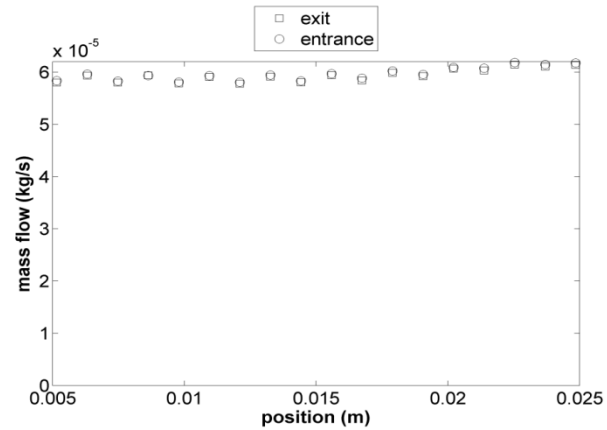


Figure 8. Plot of mass flow rate per channel versus channel position. Each data point represents the total mass flow rate in an individual channel.

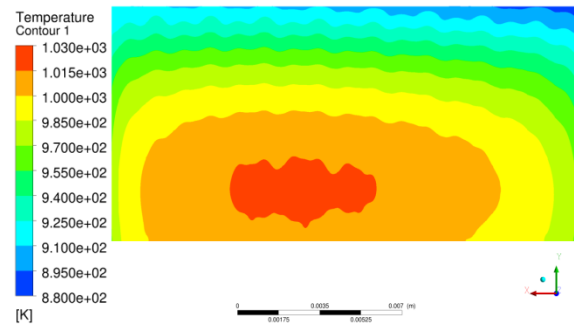


Figure 9. Temperature contour at the heated surface. The area depicted is 1 cm by 2 cm, half of the total 2 cm by 2 cm heated surface due to the plate of symmetry used. Fluid in microchannels flows from top-to-bottom.

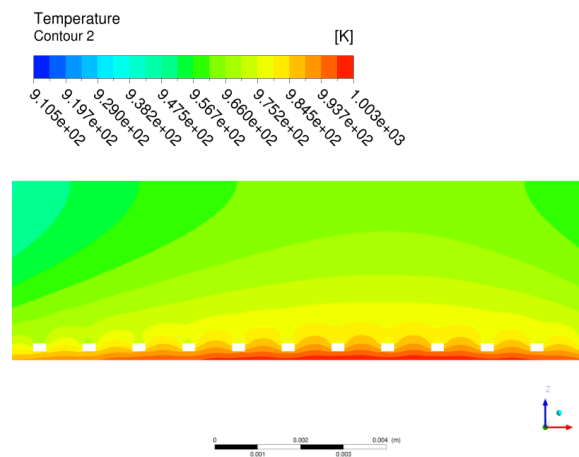


Figure 10. Temperature contour in solid at a cross-sectional plane perpendicular to the stream-wise direction in the microchannels. Solar flux is incident on the bottom edge.

area. The resulting interior surfaces of the header lead to high force on the walls header, with potential for failure, as illustrated in Figure 11. In this image, solar flux is incident on the top-most edge of the device. Fluid in the headers flows into and out of the page and fluid in the channels flow right-to-left and left-to-right (though the channels are not visible here). Failure would occur in plate-1, where the thin plate is stretched by the force on the header walls.

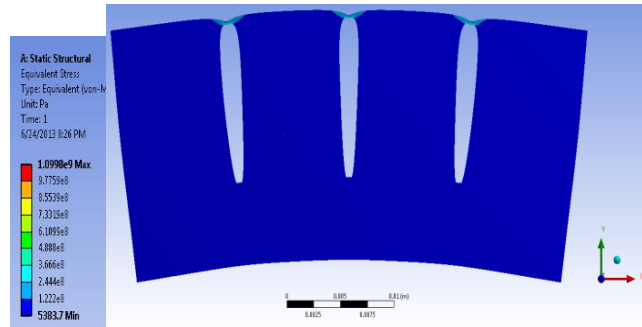


Figure 11. Exaggerated schematic of header stresses showing failure mode.

To solve this problem we divided the header into two regions: one in plate 2 and one in plate 3. In plate 2, the continuous slots are divided into nine separate slots, with ribs between the two walls of the header. The ribs take most of the stress away from plate 1. Also, the height was reduced in order to reduce the force on the header walls. Obviously, this first header region alone could not distribute the flow. This is the task of the second header region. In the final design, the highest stress results in a safety factor of approximately 1.3.

**3.1.2 Molten Salt Solar Receiver Test Article Designs**—The objective of the molten salt solar receiver test article design was to demonstrate the concept’s ability to meet the performance levels identified in milestone M1.2, which includes a molten salt exit temperature target of 600°C, assuming the development of advanced molten salts. In this section we are describing the design of our test article which is limited to and exit temperature of 550 C which represents what can be achieved today. We have completed the simulation of the 600 C and little changed in the design. Results are only summarized for the 550°C exit temperature. As with sCO<sub>2</sub>, we have selected Haynes 230 as the material of fabrication due to the combination of adequate strength at temperature, good oxidation properties, and availability.

We selected a circular pin-fin array design for the molten salt test article. The design closely follows that of Option 3 used for the sCO<sub>2</sub> test article. The goal of this design was to obtain uniform flow distribution and minimal pressure drop through the fins and to provide high efficiency for the receiver. The array was uniformly spaced and fabricated using sinker EDM; this leaves pin diameter (D) and pitch as the two design variables. A design was chosen based on a parametric simulation study that included pressure drop through the pin array and in the headers, where header pressure drop was kept to 10% of the array pressure drop to insure good flow distribution.

The full-design simulation including the conjugate problem was then performed. Table 1 lists key results. Two dimensional stress simulations were performed in two locations, the channels and the header. The internal pressure was assumed to be 5 bar.

Table 1: Key results from the full-design molten salt pin-fin simulation.

Total pressure drop	0.4 bar
Average channel wall temperature	797.1 K
Predicted heated surface temperature	838.3 K
Thermal efficiency	99.1%
Receiver efficiency	94.1%

The temperature solution from the conjugate simulation was used to approximate the temperature gradients in the areas of interest. The minimum safety factor in this simulation was 2.5.

The results of Task 1 show that based on simulation, we can achieve the level of performance documented in our milestones for both the molten salt and sCO<sub>2</sub> receiver test articles. This means that based on simulation, a molten salt receiver with an incident flux of 400 W/cm<sup>2</sup> is feasible. This is more than a factor of four better than existing technology, and we achieve the flux level with thermal losses of less than 1%. In addition, the small temperature gradient across our microchannels has basically eliminated thermal stress as an issue for the molten salt design.

We have several options for a sCO<sub>2</sub> receiver test article, all of which achieve our flux goal of 100 W/cm<sup>2</sup> with thermal losses of between 5% and 7%, while our molten salt design achieves our flux goal of 400 W/cm<sup>2</sup> with thermal losses of 1%. In both cases the thermal losses we predict are based on an open receiver and do not include any cavity effect or a cover glass. If we include reflection losses, our total receiver losses are within 1% of our milestone targets. Based on these results we conclude that we have met our milestones M(1.1) and M(1.2)

**3.2. Tasks 2 & 4- Test Article Fabrication**—Lab-scale test articles were fabricated using Haynes 230 for sCO<sub>2</sub> and 316 stainless steel for molten salt. The selection of Haynes 230 for sCO<sub>2</sub> was based on a review of a number of refractory materials. Among the reviewed materials were Inconel Alloys 800H, 800HT, 750, 751, 718 and Haynes 214, 230, 25, R41, and Waspaloy. Haynes 230 was finally selected as the material for sCO<sub>2</sub> receiver based on the constraint of availability of sheets in small quantities at reasonable cost, as well on experience in microfabrication methods needed to form the micro-features and diffusion bond layers.

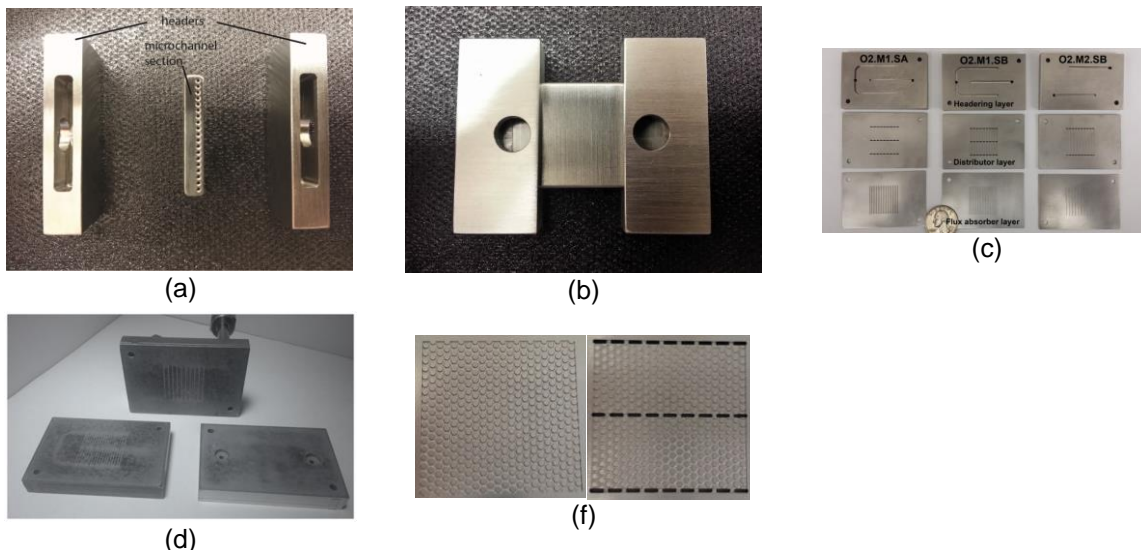


Figure 12. Examples of lab-scale sCO<sub>2</sub> receivers. (a-b) Option 1 receiver; (c) three designs of Option 2 parallel microchannel receivers; in each design, the headering, distribution, and the flux absorber layers are bonded together; (d) diffusion bonded Option 2 receivers; (e) exploded design view of the Option 3 receiver indicating the flow path; (f) flux absorber and distribution layers of the Option 3 receiver.

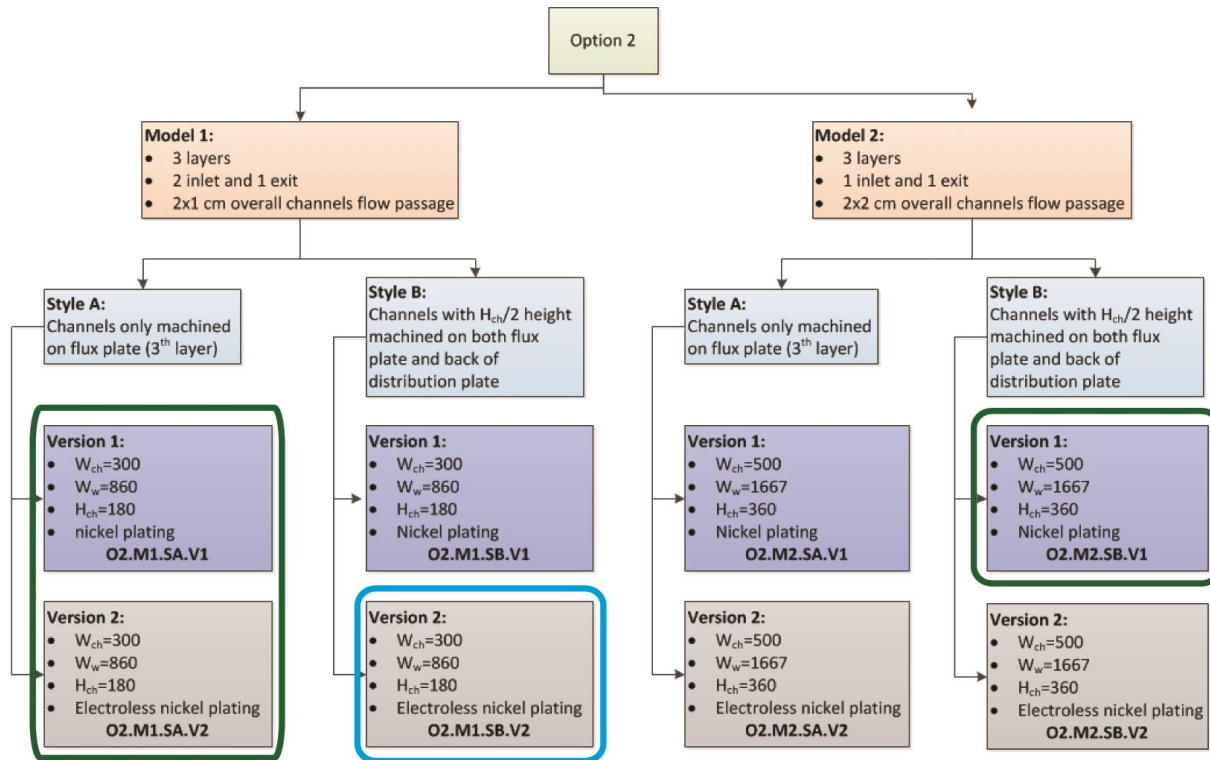
- **Option 1** - The design involves micromachining parallel circular microchannels by drilling and welding headers to the channel section. This was our low-risk option using traditional fabrication approaches.
- **Option 2** - This option consists of an array of parallel microchannels and header plates that direct fluid into and out of the array. The parallel microchannel arrays were micromachined and the plates were diffusion-bonded together to form the receiver.
- **Option 3** - In this option, a micro-pin fin array is used instead of parallel microchannels. This fabrication approach can include sinker EDM for the pin array and diffusion bonding.

**Option 1 sCO<sub>2</sub> receiver:** The Option 1 test article consisted of a microchannel section that was welded in place between two header sections. Two 6.25 mm outer diameter tubes were welded to the headers. The microchannel section was 1.5 cm long x 2 cm wide with 19 microchannels that were 500  $\mu\text{m}$  in diameter and spaced 500  $\mu\text{m}$  apart. These channels were formed by drilling into the material and were located 0.3 mm from the wall that was to be exposed to the simulated solar flux. The microchannel section was inserted within the plena and welded. The Option 1 test article was fabricated and tested for integrity in Phase 1. Because it did not involve diffusion bonding, it was the lowest risk option in terms of fabrication, and it was thus attempted first. Given the success that we had in fabricating Options 2 and 3, and the difficulty in scaling up an Option 1 design, we chose not to perform sCO<sub>2</sub> testing (Task 5) using this receiver.

**Option 2 sCO<sub>2</sub> receiver:** Five lab-scale receivers were fabricated from a matrix shown in Table 2 on the following page. The five test articles encompass different models, styles, and versions of the device necessary to provide us with guidelines for the multiple unit cell test articles to be designed and fabricated in Phase 3. Style A designs have the channels machined into one plate, resulting in a sharp corner when the plate containing the channels is bonded to the top plate. Style B involves machining channels into both the channel plate and the top plate where these channels are one half the depth of the Style A designs. Machining results in a curved radius at the end of the channel, so this approach will avoid 90° corners at the bonding interface but does require alignment of the plates during bonding. Our bonding vendor required deposition of a nickel layer on the shims prior to bonding. There were two options for deposition of the nickel layer, thereby resulting in two versions in Table 2.

As shown in Fig. 12(c), each of the Option 2 test articles consists of three plates: (a) a 400-micrometer thick flux absorber plate; (b) an intermediate fluid distribution layer; and (c) a headering layer that connects the inlet and exit plena to circular tubes. By the end of Phase 1, the three plates comprising the six Option 2 test sections had been fabricated. In Phase 2, the six test articles were bonded and pressure tested at temperature.

Table 2. Flow chart showing characteristic dimensions and features of Option 2 test sections\*.



\* Model 1 designs involve 1-cm-long channels with two inlet and one outlet headers, while Model 2 is the design with 2-cm-long channels and 1 inlet and 1 exit header. The two models will allow for comparison of scale effects in Task 5.3 between two unit cells of 2 cm<sup>2</sup> flux area (model 1) and one unit cell of 4 cm<sup>2</sup> flux area (model 2). Receivers described above bordered in dark green were bonded in the first round. Two identical receivers of the type bordered in blue were bonded in the second round along with one Option 2 receiver.

We bonded test articles in a two-stage process. In the first stage, three test articles were bonded: O2.M2.SB.V1; O2.M1.SA.V1; and O2.M1.SA.V2. The first two received sulfate-based electrolytic nickel plating and the last one received phosphorus-based electro-less nickel plating. The first test article had unit cells that were 2-cm long x 2-cm wide with one inlet and one exit header. Channels were cut to half depth on both the absorber and distributor plates. The second and third test articles had 2-cm wide and 1-cm long unit cells with two inlet headers and one exit header. In both of these test articles, channels were cut only into the flux absorber plate. Fig. 12(d) shows a photograph of the test articles from the first stage of bonding.

In the second stage, we bonded two O2.M1.SB.V2 test and one Option 3 test articles. The test articles in this bonding stage received electroless nickel plating as we had found no difference in integrity between the two coatings.

**Option 3 sCO<sub>2</sub> receiver:** This option uses a micro-pin fin array for heat transfer in the flux absorber layer. The pins were patterned using sinker EDM by an external vendor. Fig. 12(e) shows an exploded view of the micro-pin fin receiver indicating the fluid passages in and out of the receiver. Photographs of the fabricated pin fin absorber plate and distributor plates are shown in Fig. 12(f). The flux absorber plate has through-cut

inlet slots that connect to deeper plena on the back side of the distributor plate and in the header plate. The cross-sectional dimensions of the machined flux absorber plate were verified using optical profilometry. The pins were 1100  $\mu\text{m}$  in diameter and the edge-to-edge spacing between pins was 600  $\mu\text{m}$ . The depth of the pins was 160  $\mu\text{m}$  in both the flux absorber and distributor plates, making the bonded depth of the micro-pin fin section 320  $\mu\text{m}$ .

**3.2.2 Molten salt test articles**—A pin fin array was also chosen for the molten salt receiver based on simulation results in Task 1. The design closely follows that of Option 3 used for the sCO<sub>2</sub> test article. The receiver was 1 cm x 1 cm given the requirement of testing at an increased flux of 400 W/cm<sup>2</sup>. Figure 13(a) shows the fluid path through the three layers of the molten salt lab scale receiver. Two versions of this receiver were fabricated, one having three layers, identical to the sCO<sub>2</sub> receiver, and a second having two layers, wherein the headers and distributor layers were combined into one plate. Fig. 13(b) shows the fabricated layers in stainless steel using sinker EDM for the smaller features and traditional machining for the larger features. The layers were diffusion bonded in house and tested.

Initially a 2-layer design test article was installed. Under substantial N<sub>2</sub> head pressure, no flow was observed during multiple tests. After ruling out the possibility of salt blockage, the 2-layer diffusion bonded test article was replaced by a 3-layer design test article. With all heaters functioning correctly, a mass flow rate of 0.08 g/s of molten salt flow was achieved, however this was on the low end of an acceptable design flow rate.

The primary cause of the lower than expected flow was fabrication errors in the sinker EDM and diffusion bonding processes which resulted in channels that were much smaller than expected. The molten salt flow rates for the 3 layer design under reasonable supplied pressure head (.08 g/s) were too low to sustain a heat flux on the order of 400 W/cm<sup>2</sup>. Consequently, in Phase 3 of the project, new molten salt test articles were fabricated with better dimensional controls.

A model of the new test article is shown in Fig. 13(c). The new test article was designed to minimize surface area and mass, thus minimizing thermal losses. Inlet and outlet header depth and width dimensions, pin dimensions, and test region dimensions were all maintained consistent with the original design. However, the header lengths were shortened to allow for a more compact design, reducing the surface area by 30%. These design changes were intended to reduce heat losses from the test article observed during testing of sCO<sub>2</sub> test articles.

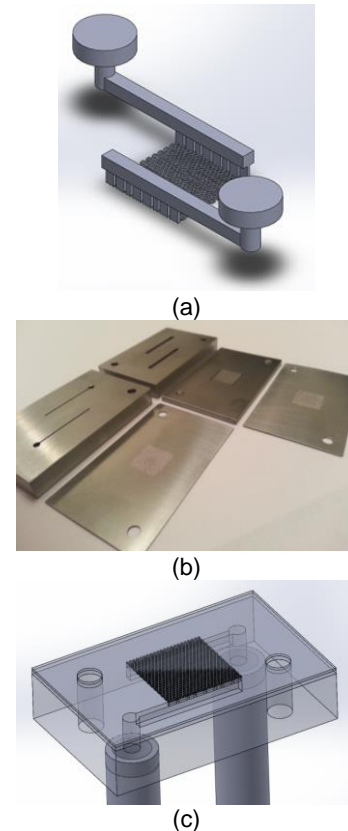


Figure 13. Molten salt receiver pin fin array.

### 3.2.3 Mechanical Integrity Testing - Test Facility and Approach

Figure 14(a) shows a schematic of the sCO<sub>2</sub> test article pressure and temperature test facility, while Fig. 14(b) shows a picture of the test enclosure. The enclosure was located within a sheet metal frame and inside a large vent hood. The test article was located within the chamber using welded inlet and exit tubes as shown in Fig. 14(a). A high pressure line from a nitrogen tank was connected to the inlet tube while the exit tube was connected to an absolute pressure transducer. A propane flame was used to heat the test section, and a thermocouple located at the back face of the test section was used to record the surface temperature. Thermocouple and pressure transducer data were recorded using a data acquisition system.

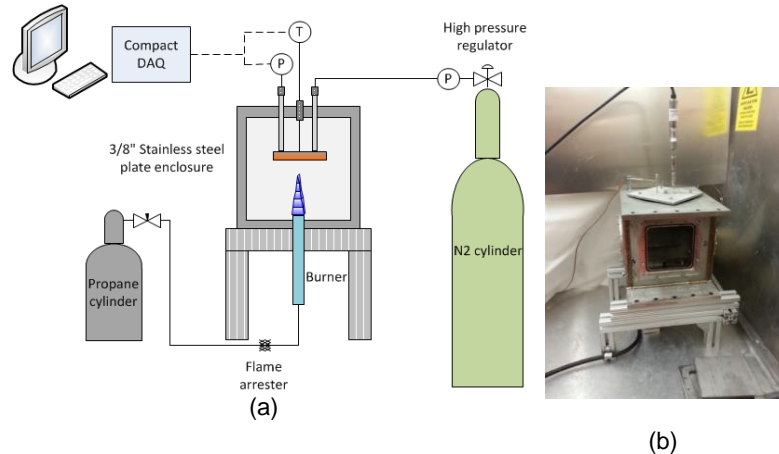


Figure 14: Pressure and Temperature testing facility (a) schematic, (b) picture of test chamber.

The testing was undertaken in three stages: (a) pressure testing up to 130 bar at room temperature; (b) temperature testing up to 800 °C at 20 bar; and (c) pressure and temperature testing at 130 bar and 800 °C, respectively. We tried to follow as much of the ASME Section VIII Div. 1 UG-101 code, as possible in preparing the test procedures.

3.2.4 Mechanical Integrity Testing- Results—Figure 15(a-f), below and following page, presents the results of static pressure testing the different sCO<sub>2</sub> lab scale receivers at their nominal operating temperatures. As can be seen for Options 1-3, all receivers successfully passed the integrity tests.

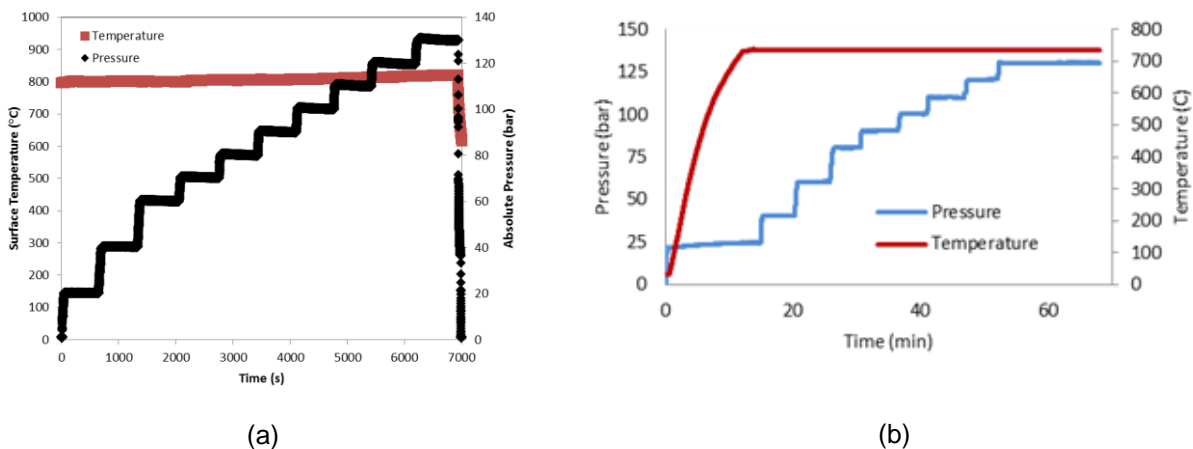


Figure 15(a-c). Results from static pressure testing at receiver operating temperatures (a) Option 1 sCO<sub>2</sub> receiver and (b) Option 2- O2.M2.SB.V1 sCO<sub>2</sub> receiver.

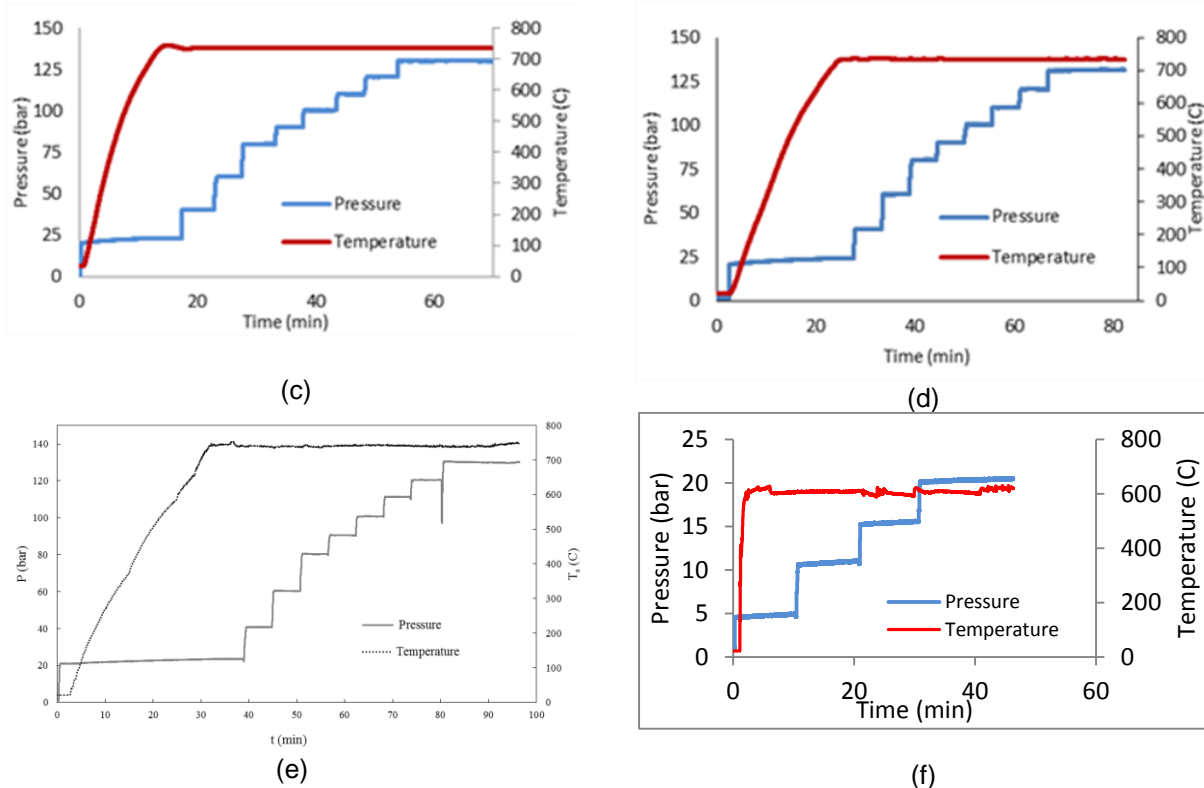


Figure 15(c-f). Results from static pressure testing at receiver operating temperatures (c) Option 2-O2.M1.SA.V1 sCO<sub>2</sub> receiver; (d) Option 2- O2.M1.SA.V2 sCO<sub>2</sub> receiver; (e) Option 3 sCO<sub>2</sub> receiver; (f) molten salt receiver.

**3.3 Task 3 – Phase 1 Separate Effects Testing (T-3):** In order to perform thermofluidic testing of the lab-scale receivers discussed in the prior section, a simulated concentrated solar test facility was developed. Two separate flow loops – one for sCO<sub>2</sub> and a second for molten salt were also assembled to interface interchangeably with the solar simulator.

**3.3.1. High Flux Solar Simulator**–Based on a literature survey and power restrictions in the laboratory, a concentrator consisting of a single 6 kW Xenon arc lamp (Osram XBO 6kW HS XL OFR) located at the focal point of a truncated ellipsoidal reflector was selected. The lamp power supply was controlled using a LabVIEW program via a 15 pin interface. Figure 16(a) shows the key components of the reflector, lamp, power supply, and cooling systems. The lamp was rigidly fixed at the base by an electrically isolated aluminum support arm. The top of the lamp was supported by a spring loaded high-temperature plastic connection to eliminate stress caused by thermal expansion were a rigid support used. In order to remain under the permissible temperature limit of 200°C, we developed a cooling system consisting of two rings of forced air jets, one aimed at the base of the bulb and the other at the top. The cathode cooling arrangement consists of a ring of copper tubing arranged around the base of the bulb, with nine drilled holes directed vertically and the flow parallel to the major axis of the bulb. A similar cooling scheme was followed for the anode. A pitot probe along with a NIST traceable pressure transducer were used to determine the velocity of cooling flow around the lamp and ensure it was in excess of the requirements stipulated by the manufacturer.

Fig. 16(b) shows a picture of the elliptical reflector surface. The design of the reflector was based on Monte-Carlo ray tracing simulations performed using TracePro® (Lambda Research). Simulations indicated that fluxes of  $\sim 100 \text{ W/cm}^2$  could be attained over a diameter of about 4 cm, and  $\sim 380 \text{ W/cm}^2$  over a 1 cm diameter. Once the reflector design was finalized, manufacturing of the reflector was undertaken in three phases at three different facilities. The rough shape of the reflector was milled out of a single 425lb block of 6061 aluminum using an in-house Fadal CNC88HS mill. The reflector was then precision diamond-turned to generate a mirror surface finish. After diamond turning the reflector was silver coated via vapor deposition.

During the course of the research, we fabricated two reflectors, the second of which had to be re-turned and coated twice. The issues leading to reflector degradation were first thermal (overheating), and next chemical corrosion during molten salt testing. The first two coatings applied by the vendor were pure silver. The third time, the vendor applied a proprietary chemical-resistant silver coating in order to prevent corrosion by molten salt vapors. The reflectivity data for the third coating is provided in Fig. 16(c).

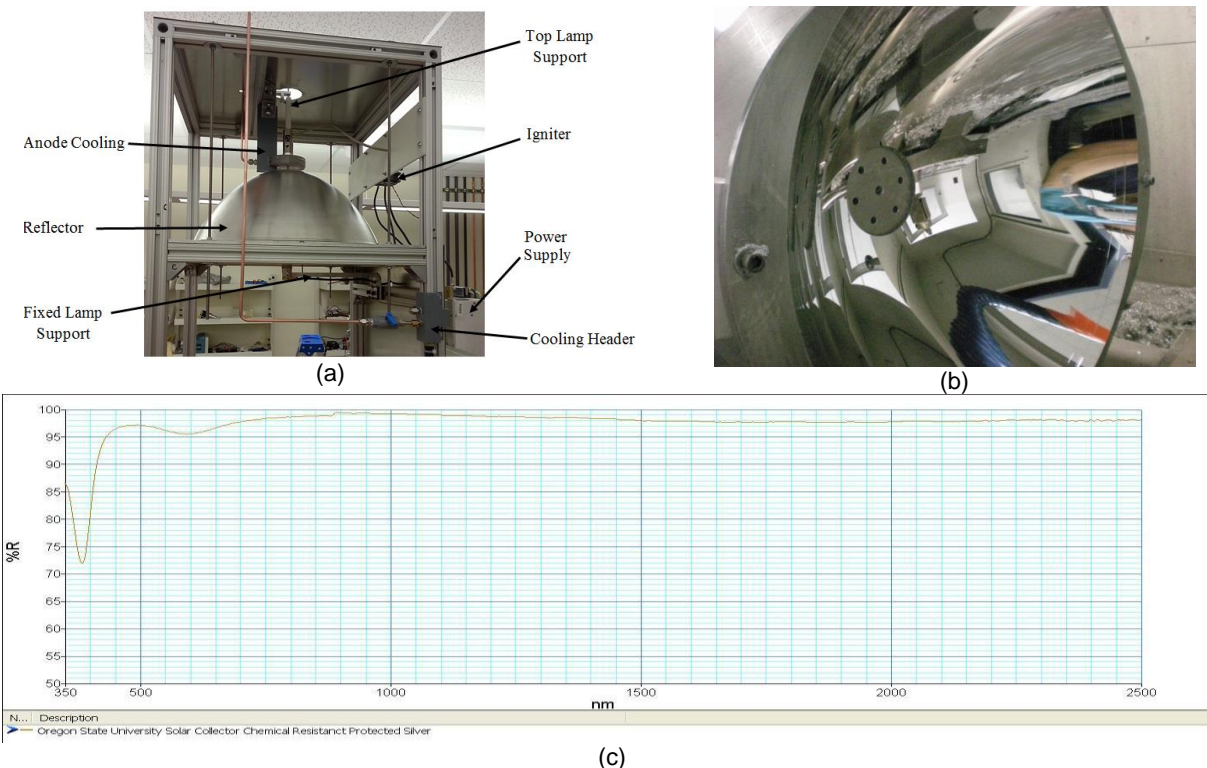


Figure 16. High flux simulated solar concentrator (a) main components of the concentrator, (b) elliptical concentrator inner surface, and (c) reflectivity data on the latest chemical-resistant silver coating on the concentrator.

Heat flux values were determined by using a water cooled Vatel TG1000-1 flux meter gauge with an AMP-15 amplifier to read fluxes ranged from 0 to  $600 \text{ W/cm}^2$ . The heat flux meter was fixed to a 28-cm x 28-cm water-cooled aluminum plate and mounted to a stage that was connected to a 2D stepper-motor controlled traverse. This traverse is controlled using a LabVIEW program that specifies the area over which heat flux measurements are to be recorded. Alternately, a custom-built water-cooled heat flux meter

was also used to check the area-averaged heat flux values obtained from the Vatel fluxmeter.

**3.3.2 sCO<sub>2</sub> Loop**—The supercritical test facility is shown schematically in Figure 17. sCO<sub>2</sub> is pressure-driven through the open loop using a helium-headed sCO<sub>2</sub> cylinder. Liquid CO<sub>2</sub> at supercritical pressure was heated in two stages: first, the liquid is heated to ~50°C in a hot oil bath and subsequently heated to ~400°C in a custom-built pre-heater. Supercritical pressure within the test section was maintained using two high-pressure regulators. The first regulator was used to adjust the cylinder pressure to the desired test condition. A second pressure regulator was used to maintain the pressure in the receiver section of the facility and reduce the CO<sub>2</sub> pressure to near atmospheric at its exit prior to the flow meter. An absolute pressure transducer was located on the second regulator entrance to measure the line pressure. A dial pressure gauge located on the exit of this regulator was used to monitor the downstream pressure. Past the receiver and prior to the second pressure regulator, the temperature of the fluid was reduced in a water-cooled heat exchanger. A fine-turn needle valve with a Vernier handle was used to control the flow rate through the test section. Downstream of the valve, the gas was cooled to around 40°C before entering the pressure regulator. A calibrated Brooks mass flow meter was used for measuring the CO<sub>2</sub> flow rate. Data from the flow meter, pressure transducer, and thermocouples were read directly into LabVIEW (National Instruments) data acquisition software.

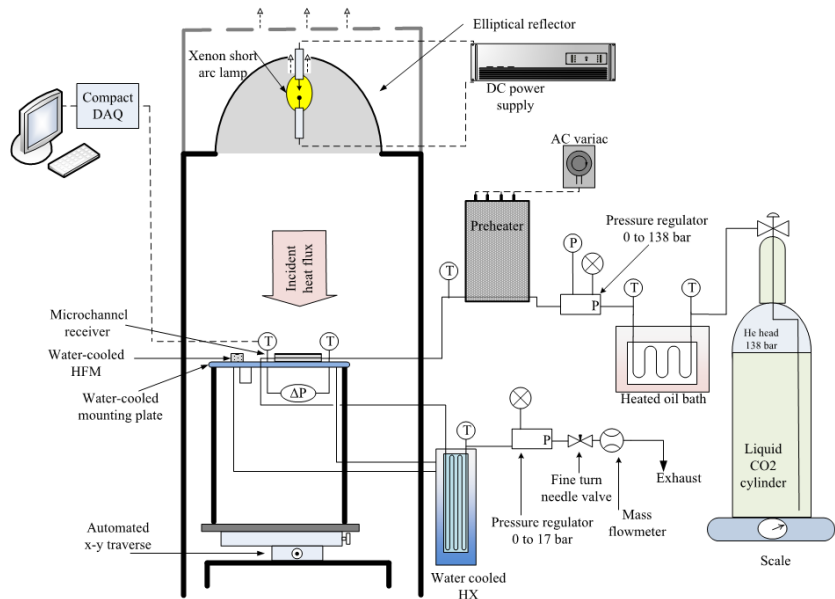


Figure 17. Schematic of the sCO<sub>2</sub> test facility.

A calibrated Brooks mass flow meter was used for measuring the CO<sub>2</sub> flow rate. Data from the flow meter, pressure transducer, and thermocouples were read directly into LabVIEW (National Instruments) data acquisition software.

In order to provide concentrated flux only over the 2 cm x 2 cm area, a 21-mm x 21-mm water-cooled flux mask was located 1.5 cm above the receiver as shown in Figure 18.

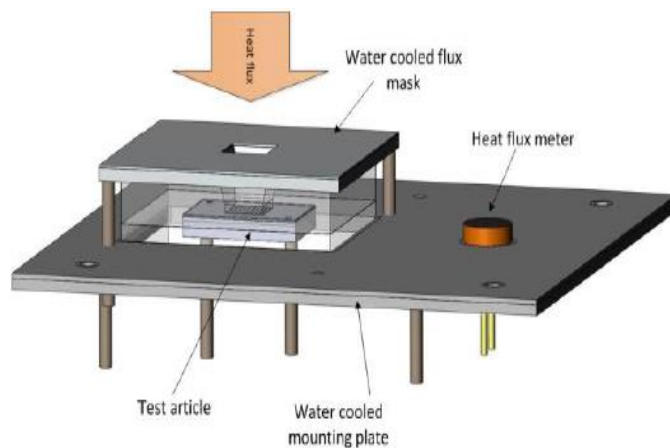


Figure 18. Solid model of the test article with the water cooled flux mask.

Seven thermocouples were located on the body of the receiver and in the

inlet and exit tubes and their locations are indicated in Fig. 18. Four of these thermocouples were located under the insulation on the side of the receiver that received the concentrated flux. An average of these four thermocouples was considered as representative of the receiver surface temperature.

**3.3.3. Molten Salt Test Loop**—The open-loop molten salt test facility is shown schematically in Figure 19. The molten salt used was Dynalene MS-1 with recommended operating range between 285 and 550°C. The high freezing temperature of the salt (237°C) coupled with low mass flow rates through the loop salt, imposed strict thermal regulation constraints in the design of the test loop. The 6-liter stainless steel molten salt reservoir was heated using four high-temperature band heaters that were controlled using AC variacs. The molten salt was pumped through the loop using a pressurized head of nitrogen on the reservoir. A precision turn regulator for the nitrogen was used to provide fine control of the molten salt flow rate. The pressure head causes the molten salt to exit the reservoir through a draw tube. Nitrogen also acted as an inert gas blanket to prevent oxidative degradation of the molten salt as well as reduce metal corrosion. Thermocouples were used to monitor the temperature of the molten salt and the exterior surface of the reservoir. The flow rate was determined using a catch-and-weigh technique by collecting exiting molten salt from the receiver onto a glass beaker atop a precision mass balance. A computer-controlled pneumatic actuator was used to switch between an exit reservoir and the beaker. Since the timing of the actuator was controlled via a computer, accurate time of mass collection, down to the actuator response time of 1 s was achieved.

Upon exiting the receiver, in order to prevent refreezing of the salt prior to mass collection, a jacket of molten salt was used to keep the salt above the freezing point as shown in Fig. 19. In addition to four band heaters on the tank, initially four additional band heaters were used on the molten salt jacket to keep the molten salt above its melting temperature. Furthermore, two rope heaters were used to preheat the tubing section entering and exiting the test article.

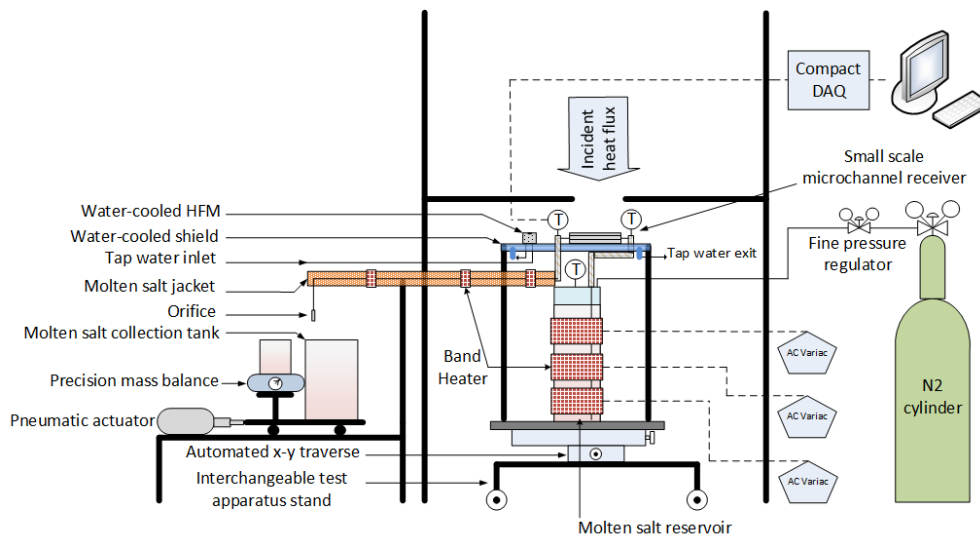


Figure 19. Schematic of the modified molten salt loop.



Figure 20. Current molten salt test facility (left); test article and heating jacket zoom in (right).

Figure 20 shows pictures of the final molten salt test loop. Despite the efforts described above, some cold spots within the loop could not be eliminated. A simpler, more robust thermal regulation system was therefore developed. This heating system is shown in Figure 21. It utilizes a custom built heater made of brass. Two blocks of brass were machined to allow flow to and from the test article, with thermocouple ports to measure salt temperature very close to the test article inlet and outlet. The brass was heated with several 1/4" cartridge heaters. Each block's temperature was monitored and individually controlled by separate power sources in order to maintain a similar temperature to that of the salt leaving the reservoir.

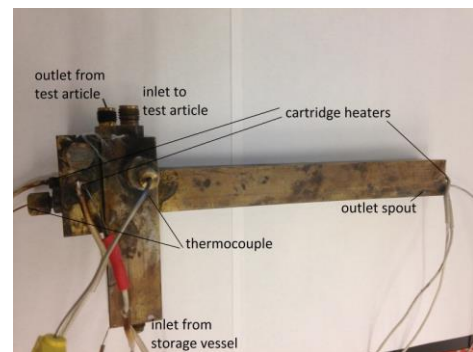


Figure 21. Current brass heating system for molten salt experiment.

**3.4 Task 5 – Phase 2 Separate Effects Testing (T-5):** In this section of the report, results of the sCO<sub>2</sub> and molten salt lab-scale receiver tests are presented. It is shown that receiver thermal efficiencies in excess of 90% at absorbed fluxes of ~100 W/cm<sup>2</sup> is possible with sCO<sub>2</sub> as the working fluid. Relative to our molten salt test article. Due to a number of equipment problems we have not yet been able to achieve incident fluxes of 400 W/cm<sup>2</sup>. Currently we have reached incident fluxes of 150 W/cm<sup>2</sup> where we have an experimentally determined receiver efficiency of 70%. This is for a receiver without an optical coating. The results are consistent with a receiver efficiency between 90% and 95% for a flux of 400 W/cm<sup>2</sup> and using a coating with the properties of Pyromark. We expect to have results for the molten salt test article operating at 400 W/cm<sup>2</sup> in two or three weeks.

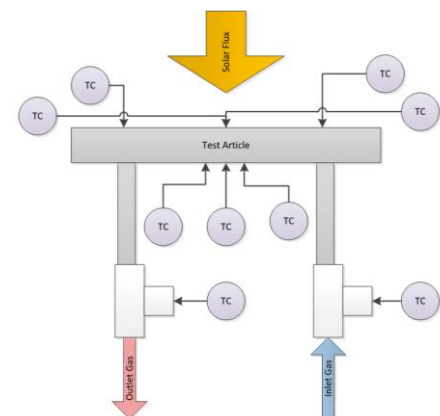


Figure 22. Thermocouple placement on the lab-scale receiver.

**3.4.1 sCO<sub>2</sub> Results and Discussion**—Figure 22 is a schematic of the sCO<sub>2</sub> test article showing the location

of the surface and fluid measurement thermocouples. During preliminary tests with the lab scale test article we found that heat loss on the order of 10% of incident heat occurred through the insulation. The heat loss was largely a result of the small ratio of the surface area for incident flux to that of the test section. Since in a commercial scale receiver such insulation losses can be minimized, if not eliminated, we chose to modify the thermal and receiver efficiency definitions to account for the insulation losses. Efficiency numbers, corrected for such thermal losses through the insulation, would be more representative of the commercial scale receiver efficiencies that can be obtained using microchannels. The inefficiencies would then arise solely due to the re-radiation and convective losses from the surface of the receiver that is exposed to the simulated solar flux. Upon correction for heat losses, a modified receiver efficiency is defined as the heat gained by the fluid to the net heat incident on the receiver (Eqn. 1),

$$\eta_{rec,exp} = \frac{q_{fluid}}{q_{in,net}} = \frac{\dot{m}_{sCO_2}(h_{out} - h_{in})}{q_{incident} - q_{loss}} \quad (\text{Eqn. 1})$$

where the net heat is determined by subtracting thermal losses from the incident heat rate. Similarly, the modified thermal efficiency was defined as (Eqn. 2)

$$\eta_{th,exp} = \frac{q_{fluid}}{q_{abs,net}} = \frac{\dot{m}_{sCO_2}(h_{out} - h_{in})}{\alpha q_{incident} - q_{loss}} \quad (\text{Eqn. 2})$$

In order to estimate heat losses through the insulation, a separate heat loss calibration experiment was performed for each of the lab-scale test articles. A schematic representation of the test facility for heat loss calibration is shown in Figure 23. The upper 2cm x 2cm surface of the receiver that is exposed to concentrated radiation in the sCO<sub>2</sub> experiments was thoroughly insulated for the heat loss experiments. The remainder of the receiver insulation was identical to that during the sCO<sub>2</sub> tests. Heated nitrogen gas was flowed at a metered flow rate through the receiver and the drop in temperature of the gas at the exit of the receiver at steady state was noted allowing determine the heat loss. The seven thermocouples located on the body of the receivers were averaged to represent the body temperature at which the heat loss was determined. Figure 24 shows a plot of estimated heat losses as a function of this average body temperature. A best fit curve that represented the data was used

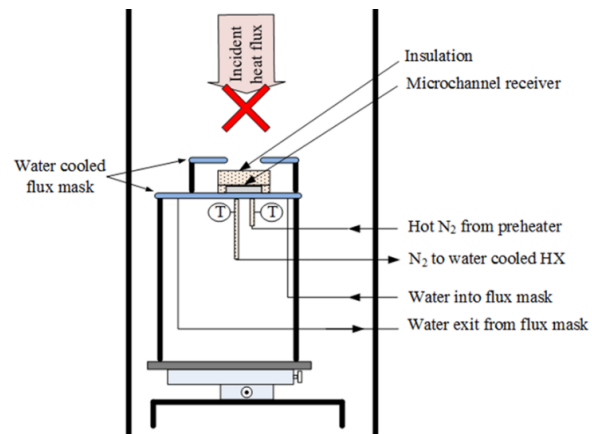


Figure 23. Schematic of the facility for in-situ heat loss calibration. The entire receiver was insulated and no concentrated flux was applied.

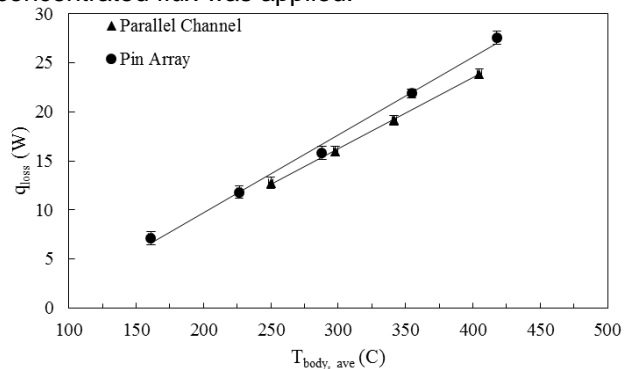


Figure 24. Heat loss calibration curve for the Option 2 and Option 3 receivers.

to estimate heat losses in the sCO<sub>2</sub> experiments. Note that the curve fit is linear, indicating that heat loss was by conduction through the insulation. The heat loss experiments were restricted to temperatures of ~400°C, the highest gas temperature possible with the preheater. However, since the curve fit was linear, the heat loss projections were extrapolated to higher surface temperatures (600°C-750°C) seen in actual experiments. The slight difference in slope of heat loss between designs is attributed to the variation of insulation during setup of the two separate experiments.

Initially an optical coating, Pyromark 2500, was applied to the receiver surface. During testing, the coating began to degrade and provided unreliable surface reflectivity. Since no other alternative was readily available at the time of testing, the receiver surface was lapped to bare Haynes 230. As will be shown in section 3.7, a method of applying Pyromark 2500 onto Haynes 230 was successfully implemented in Phase 3 of the project. To fully discolor the surface, a burn-in cycle of the surface was performed by running the high flux experiment first until steady state. Once data collection for both heat loss and efficiency was complete, the reflectivity of the bare Haynes was assessed using a spectrophotometer (JASCO UV-670), with a manufacturer stated accuracy of 0.3% for transmittance measurement and 0.05 nm for wavelength. Reflectance was measured at room temperature and at a single angle of approximately 10° off normal. In order to obtain a surface reflectance, the device was cut using wire EDM so the channel section could be placed into the spectrophotometer part holder. Numerical integration of the device surface reflectivity and the spectral variation of irradiation from the Xe arc lamp provided a spectrally-averaged reflectivity of the device (Eqn. 3),

$$\rho_{Haynes} = \frac{\sum(\rho_{\lambda, Haynes} \cdot E_{\lambda, Lamp} \cdot d\lambda)}{\sum(d\lambda \cdot E_{\lambda, Lamp})} \quad (\text{Eqn. 3})$$

To perform the integration, an eight term Fourier curve fit was generated using Matlab's built-in curve fitting software applied to the Haynes reflectivity data. This curve fit was then used to numerically integrate at the same wavelengths as the lamp output. Curves of spectral dependence of reflectivity and lamp irradiation are shown in Figure 25. The integration provided a  $\rho_{Haynes}$  of approximately 0.172. The absorptivity, for use in Eq. 2, was evaluated based on this surface reflectivity and the assumption of opacity of the surface.

**Uncertainty Analysis:**

Thermocouples reading the fluid temperatures were calibrated using a NIST-traceable hand held calibrator (Omega, PCL-1B) as a standard. The calibration error included errors associated with the calibrator, the calibration precision error and the curve fit

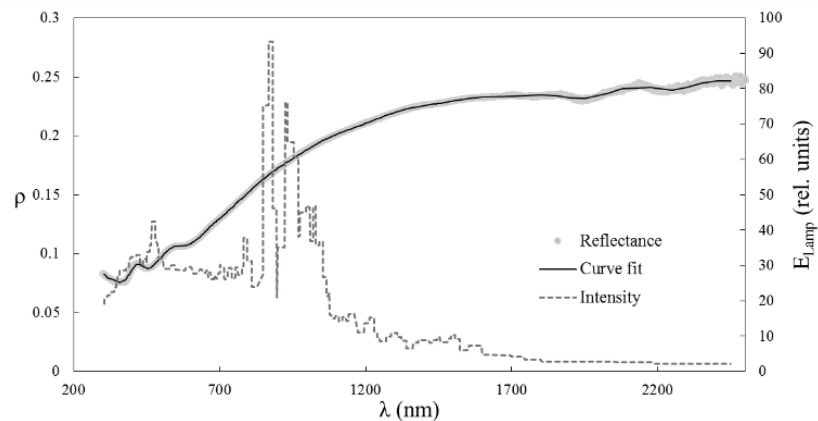


Figure 25. Spectral dependence of bare Haynes 230 surface reflectivity and lamp output.

error. The differential and absolute pressure transducers and both the volumetric and mass flow meters were factory calibrated.

The Kline and McClintock error propagation method was used to determine uncertainties in the calculated parameters based on the bias and precision errors of the measured variables. Uncertainties in measured parameters were obtained by combining the measurement precision calibration errors in a root-sum-square manner. Engineering Equation Solver (EES, Fchart Inc.) was used to perform the propagation of errors. Maximum uncertainty in measured variables was propagated into the dependent variables. Representative measurements of the uncertainty are provided in Table 3.

Table 3. Representative measurement uncertainty estimate

Measurement	Maximum Uncertainty ( $\pm$ )
Volumetric flow rate (N <sub>2</sub> )	$\pm 0.115$ slpm (0.32%)
Mass flow rate (sCO <sub>2</sub> )	$\pm 0.0114$ g/s (1.0%)
Average gas temperature	$\pm 0.46$ C (0.12%)
Surface temperature	$\pm 2.81$ C (0.4%)
Heat flux	$\pm 4.5$ W/cm <sup>2</sup> (6.17%)
Absolute pressure	$\pm 0.35$ bar (1.63%)
Pressure drop	$\pm 0.004$ bar (6.28%)

**Pressure Drop:** Pressure drop for the pin fin array was experimentally obtained using a high line pressure differential pressure transducer (Validyne P55E-1N246S4A). Pressure drop experiments were run separately from efficiency experiments to reduce heat loss in the latter. Flow was held at approximately 100°C to ensure the gas was above critical temperature and pressure was matched to that used in efficiency experiments. As can be seen in Figure 26, the pressure drop increases with an increase in mass flow rate. The pressure drop is also plotted against Reynolds number based on hydraulic diameter,  $Re_{D_H}$ , for reference. For typical heat transfer experiments, where the flow rate is about 1 g/s, the pressure drop across the receiver is under 0.5 bar. Similar pressure drops can be expected in larger scale receivers since the flow through the micro pin fin regions occur in a parallel network. It is also important to note that, based on  $Re_{D_H}$ , the flow is expected to be in the transitional to turbulent regime through the pin fin receiver. Given that most of the correlations for pressure drop and heat transfer rate in micro-pin fin heat sinks have been developed for the laminar flow regime, there is a need for expanding the correlation database to cover the transitional and turbulent regimes as seen with the present sCO<sub>2</sub> receivers.

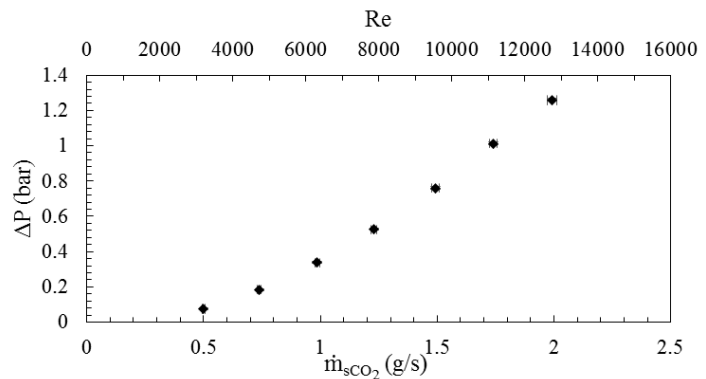


Figure 26. Experimental pin fin array pressure drop.

**Heat Transfer Experiments:** The parallel channel and pin-fin array receivers were characterized for efficiency in the sCO<sub>2</sub> test facility. Figure 27 summarizes the experimental runs performed for these receivers. Two main parameters were varied: the incident flux at a fixed fluid exit temperature [Figure 27(a)], and fluid exit temperature at a

fixed input flux [Figure 27(b)]. In all experiments the inlet fluid temperature was maintained at approximately 400°C and the receiver pressure was maintained between 81-86 bar.

As shown in Fig. 27(a), both thermal and receiver efficiency are seen to increase with increasing heat flux. The thermal efficiency for the parallel channel varies from 89.9% at 68.1 W/cm<sup>2</sup> to about 96.6% at 120.3 W/cm<sup>2</sup>, while the receiver efficiency increases from 71.7% to 78.4% over this same range of heat fluxes. The thermal efficiency for the pin array receiver is largely constant around 94% with variation in heat flux from 73 W/cm<sup>2</sup> to 120 W/cm<sup>2</sup>. With an increase in irradiation, the amount of heat transferred to the working fluid increases; however there is not much variation in surface temperature. The negligible change in receiver surface temperature results in a negligible variation in re-radiation and natural convective losses from the 2cm x 2cm exposed area. However, since the flux is increasing, an increase in efficiency with incident heat flux increase is observed, as per Eq. 2. The ability to be able to absorb high incident fluxes at a fixed surface temperature is a crucial advantage of the microchannel receivers.

It should be emphasized that the receiver efficiency is for a bare surface and not with a high absorptivity coating. Since the intent was to demonstrate that the use of microchannels permits removal of high incident fluxes at high efficiency, the metric that really matters is the thermal efficiency, since this is independent of the receiver coating. Fig. 27(b) shows the variation of thermal and receiver efficiency for a fixed input heat flux but varying exit temperatures. The exit temperature variation is caused in experiments by varying the mass flow rate of sCO<sub>2</sub>. Variation in the exit temperature for a fixed inlet temperature and input heat flux caused changes to the surface temperature. Lower exit temperatures result in lower surface temperatures, and thereby increased efficiencies as per Eq. 2. The trend in Fig. 27(b) shows that commensurate with this increase in surface temperature, a reduction in thermal and receiver efficiency is observed due to increased losses. The thermal efficiency of the pin array drops from 95.5% at a receiver exit fluid temperature of 606°C to 89% at an exit fluid temperature of 735°C. The thermal efficiency of the parallel channel drops from 98.3% at a gas exit

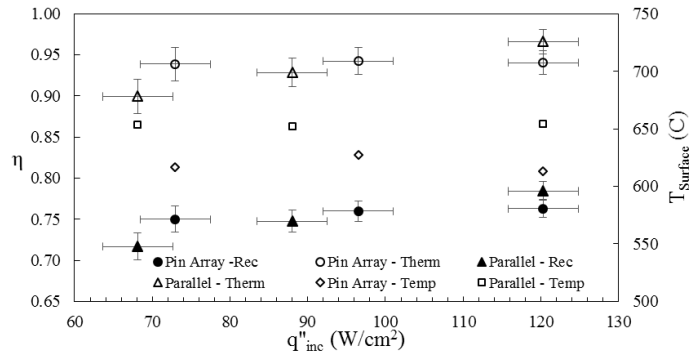


Figure 27(a). Receiver and thermal efficiency with variation of incident flux at a fixed exit temperature of ~ 650°C. Also plotted is the average surface temperature of the device.

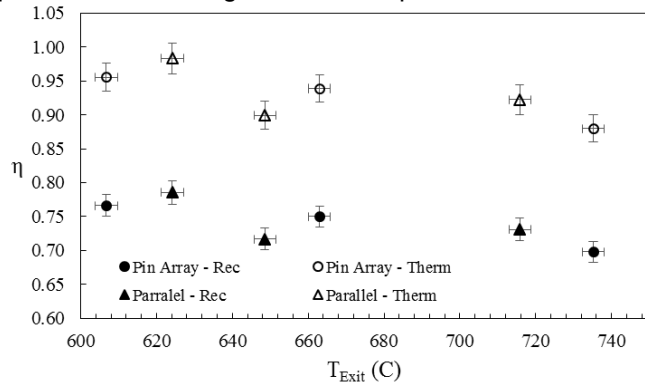


Fig. 27(b). Receiver and thermal efficiency variation with exit temperature at a fixed incident flux of 68.1 W/cm<sup>2</sup> for the parallel channel and 72.95 W/cm<sup>2</sup> for the pin array.

temperature of 624°C to 92.2% with an exit temperature of 715°C. The non-uniform drop in efficiency for the parallel channel as compared to the pin array is likely due to experimental error in the data at a surface temperature of 650°C. Regardless, thermal efficiencies of around or above 90% was achieved for both MSR designs at exit fluid temperatures of 735°C. The ability of the microchannel receiver to reduce the diffusion resistance in the fluid results in a reduced surface temperature for a fixed flux resulting in an increased efficiency.

In summary, the ability of both Option 2 and Option 3 receiver designs to absorb fluxes as high as 100 W/cm<sup>2</sup> with thermal efficiencies in excess of 90% was demonstrated. Several such receiver units could be connected in parallel through appropriate fluidic headers to create a large scale commercial microscale receiver. Pressure drop through the pin fin lab scale receiver has been shown to be under 0.5 bar, which is about 0.5% of the inlet pressure of the fluid for commercial receivers.

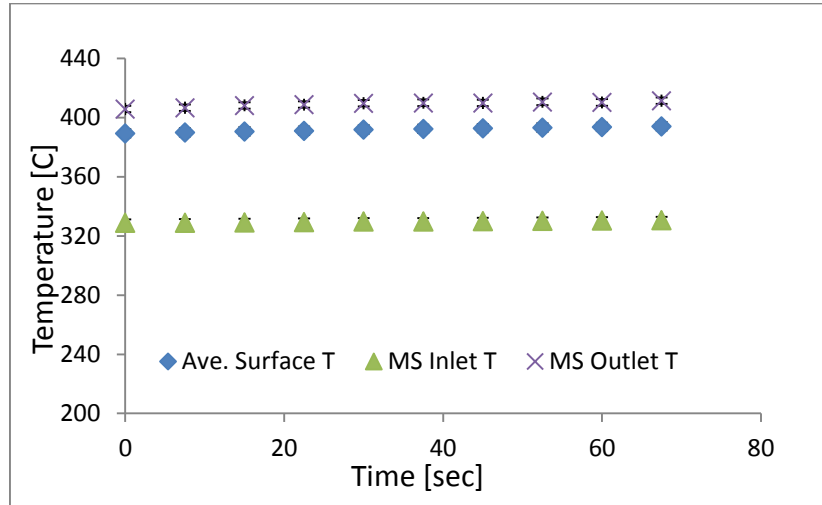


Figure 28: Molten salt temperatures under 83 W/cm<sup>2</sup> flux with a flow rate of 0.43 g/s.

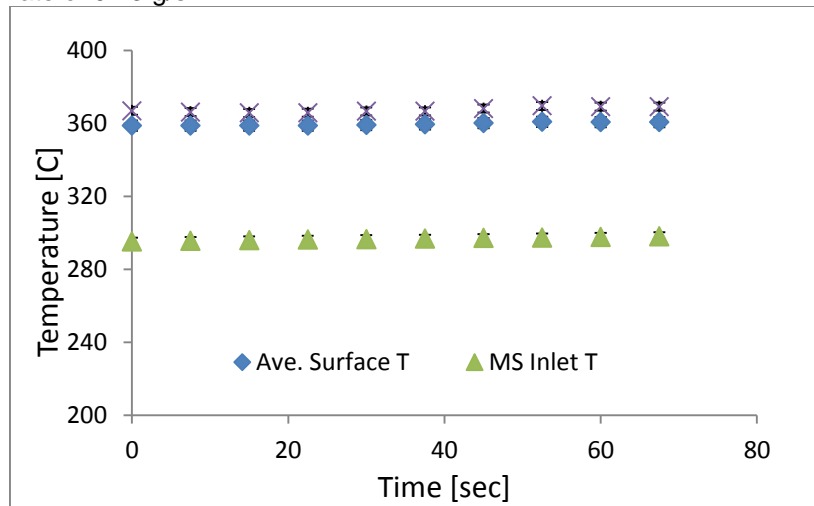


Figure 29: Molten salt temperatures under 150 W/cm<sup>2</sup> flux with a flow rate of 0.879 g/s.

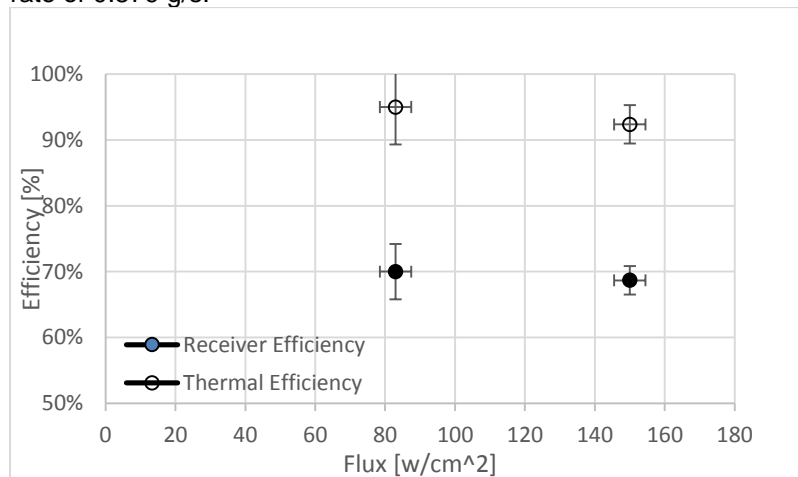


Figure 30: Molten salt receiver efficiency (bare metal, no coating) and estimated thermal efficiency under different solar heat flux.

**3.4.2. Molten Salt Results and Discussion**— We have encountered significant experimental challenges associated with testing the molten salt test article. These include the challenges associated with preventing the salt from freezing and the degradation of the flux generator, apparently caused by salt corrosion. These issues have been resolved and we have successfully collected preliminary data on the molten salt test article. We were planning to run our final tests at  $400 \text{ W/cm}^2$  incident flux and at a molten salt exit temperature of  $550^\circ\text{C}$  in June but our power supply for the flux generator failed. This is a special power supply required to operate the lamp in the flux generator and was shipped to the vendor for repair. We hope to have the device returned to OSU in the next few weeks and we will then complete testing at  $400 \text{ W/cm}^2$ . To avoid damage to our new reflector, preliminary testing was conducted with the corroded reflector which limited the incident flux that could be attained. The results presented below are preliminary data taken at lower fluxes and temperatures that will be used in our final testing but they do demonstrate the technical feasibility of the concept and are consistent with the projected performance of the device operating at higher incident fluxes and temperatures.

Molten salt tests were first performed at lower heat fluxes and molten salt temperatures owing to the degradation of the reflector. Figure 28 shows time series data from one test with the average incident heat flux over the  $\text{cm}^2$  test section of  $83 \text{ W/cm}^2$ . Although keeping constant molten salt flow has been a major challenge, the salt flow rate was fairly stable during that recording period, as indicated by the stable temperatures. However the measured receiver efficiency of approximately 70% is significantly below the expected values of over 90%. The low efficiency was caused by: 1) the test article was not coated with a high absorptivity optical coating and had 17 to 25% reflection losses, 2) The flux was approximately one fifth of the design flux and 3) conduction losses through the test article insulation. Conversely the test article was being tested at a molten salt temperature well below our design temperature. Figure 29 shows one of the tests with salt flow rate of  $0.879 \text{ g/s}$  but the heat flux was increased to  $150 \text{ W/cm}^2$  over the  $1 \text{ cm}^2$  test area (this is the maximum heat flux attainable by the corroded reflector). As shown, the salt entered the receiver at around  $290^\circ\text{C}$  and exited from the receiver at around  $370^\circ\text{C}$ . The averaged receiver efficiency was also around 70%.

Since proper processes of coating test articles with Pyromark were identified, the current molten salt test article has been coated for further testing. In addition, the team is in the process of getting the bare surface reflectivity for the molten salt test article so that the thermal efficiency of the test article can be calculated. With assumption of 25% reflectivity or 75% of absorptivity during the tests, the estimated molten salt receiver thermal efficiencies and measured efficiencies for two different incident fluxes are plotted in Figure 30.

After the previous data was obtained, the new reflector was installed so that tests could be performed with a  $400 \text{ W/cm}^2$  average heat flux. New flux maps were generated in order to determine how much power to supply to the lamp in order to get the desired  $400 \text{ W/cm}^2$  flux. Unfortunately, the power supply for the lamp failed near the end of this data collection period. It was determined that a several inductors had overheated, which might have led to the failure. The power supply was then sent to the manufacturer for repair and will be back in 1 to 2 weeks. When it returns, a final flux map will be generated to establish the flux/power relationship. After that, the final tests will be conducted

with higher flow rates commensurate with the desired average  $400 \text{ W/cm}^2$  flux and exit temperature of  $550^\circ\text{C}$ .

### 3.5 Task 6 - Integrated Test Article Design and Fabrication (T-6):

The intent of this test article was to demonstrate that the flow headers to multiple unit cells could be designed to ensure satisfactory mechanical integrity and flow distribution amongst unit cells. A three layer pin-fin design was used for the  $8 \times 8 \text{ cm}^2$  test article wherein two plates were used for flow distribution headers and the third was the micro-pin fin flux absorber plate. Each unit cell was 4 cm long x

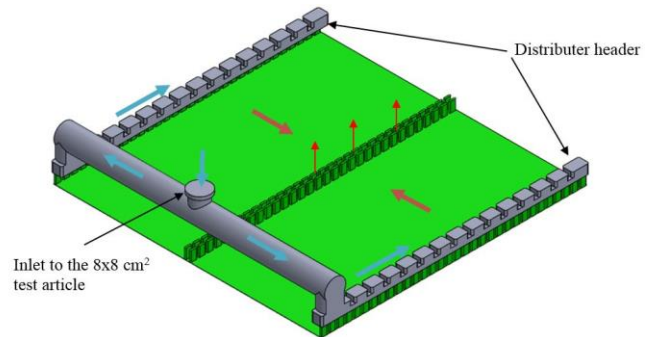


Figure 31. Fluid passage in a concept with 2 unit cells with a micro gap as simplified receiver plate

8 cm in depth in this design. In order to have uniform flow distribution in the pin array, the pressure drop in the distributor headers needs to be significantly smaller than that of across the pin fin arrays. The fluidic design of a 2-unit cell test article is shown in Figure 31. The dimensions in the distributor headers were selected based on two criteria. First, in order to distribute flow, the headers need a significantly larger flow area than in the pin array (more than 5 times). Second, they need to contain the pressure difference between 200 bar internal pressure and atmospheric outside pressure. To address the latter, the distributor headers were designed with ribs to reduce the stress.

The final design for the header resulted in a pressure drop of 14.5 kPa between the inlet into the side header and the farthest inlet to the receiver plate. The pressure drop was calculated assuming that  $\text{sCO}_2$  enters into the test section at  $500^\circ\text{C}$  and 200 bar and exits at  $650^\circ\text{C}$  with mass flow rate high enough to dissipate  $100 \text{ W/cm}^2$  absorbed heat flux. As mentioned earlier, to ensure having uniform flow distribution across the pin array, pressure should be larger ( $\sim 10$  times) than the pressure drop in the distributor header. This increase in unit cell pressure drop can be achieved by either increasing the length of unit cell or decreasing the height of pin fins. Fluent simulation was performed to determine the right dimensions for the unit cell. For the 4 cm wide unit cell and 200  $\mu\text{m}$  pin fin height the simulations showed about 176.5 kPa pressure drop, which is  $\sim 12$  times larger than the pressure drop through the header. The square pin fins had 500  $\mu\text{m}$  width and were spaced with a 1000  $\mu\text{m}$  pitch in both transverse and longitudinal directions. Hence, the final design for the test section had 2 unit cells with 8 cm length and 4 cm width.

The exploded view of the finalized design which was sent out for fabrication is shown in Figure 32(a) (from top) and b (from bottom), following page. The laminae of the fabricated test section also are shown in Fig. 32(c). Surface profilometry was performed on the fabricated plates to ensure the dimensions of the machined parts were in agreement with the designed model.

Prior to bonding the machined parts, the plates were sent out for electrolyte coating. The coated plates then were diffusion bonded by Refrac Systems. In order to provide inlet and outlet to the test section two quarter inch outer diameter H230 tubes were welded on top of the provided holes in the test section's header. Initial pressure testing with 80 psig pressurized air showed significant leaks from the edges of the test section and at the locations of the welded tubes. The heat generated by welding apparently caused the bond to fail and we had excessive surface roughness at the edges of the test article.

The 8x8 cm<sup>2</sup> test article was redesigned to eliminate these problems. Surface finish on the side edges of the receiver plate where the bond occurs between receiver plate and the flux plate was identified by the bonder to be critical.

We had used wire EDM machining fabricate the micro pin fins and this process resulted in several imperfections on the side edges. Visible grooves with depth even as high as 20 μm were found at several location on the side edges of the receiver plate. Polishing was performed with fine grit sand paper prior to bonding the first test article, but apparently not all imperfections were eliminated. Modifications were made to the new test article to eliminate imperfections at the edges. One design change is that the pin fins' base height is now different than the level of the edges. This design change would provide enough room for the wire to do the machining of the pin fins without touching the polished edges. The second major design problem was to have all distributor and collector header machined into one plate in the 3-layer test section design.

As shown in Figure 32, in order to split the inlet flow into the side headers a hole was drilled from the side of thick (14 mm) header plate. The hole then was supposed to be capped off by welding. The thermal shock (expansion and contraction) of the welding process on the side hole showed a significant stress on the bonded laminates. This led to the local failure of the bond. This problem was addressed by going to a four lamina design shown in Fig. 33. The channel for splitting the inlet flow between headers can be machined in the most top plate without any need for welding. The new device has

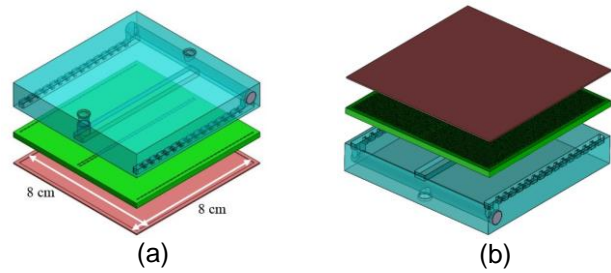


Figure 32. (a) and (b) are exploded views of the finalized design from top and bottom and (c) shows the laminae of the fabricated test section.

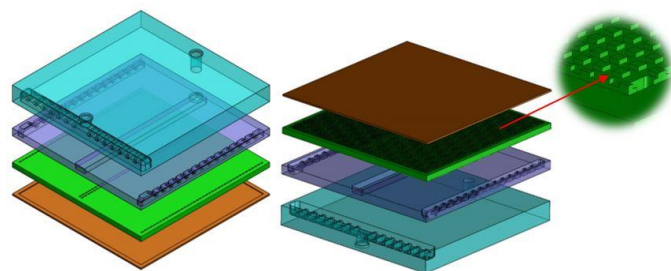


Figure 33. Exploded views of the modified design sent out for fabrication from top and from bottom with a zoom in showing the difference in the height of pin fins' base and edges on the receiver plate.

been patterned using sinker EDM and as of July 15<sup>th</sup> the test article is at the diffusion bonding contractor for bonding. We expect to receive and pressure test this device at 200 bars before the final presentation on July 28<sup>th</sup>.

**3.6 Task 7 Optical Coating Selection (T-7)** – We contacted the research groups suggested by DOE Sunshot program manager—Dr. Jifeng Liu, Dartmouth College, and Dr. Sungho Jin, University of California, San Diego—about having coupons and microchannel receiver test articles coated with a high temperature high absorptivity coating. Dr. Liu indicated that his coating has only been tested up to 650°C for 2 hours and he has not used a nickel superalloy as the substrate. He did offer to coat test coupons for us. Dr. Jin was optimistic that his coating approach could meet our needs; however, he had not worked with nickel superalloy substrates. We decided to work with Dr. Jin’s group as we felt that they were further along in developing a coating that would meet our needs. Dr. Jin’s team coated two 1.2x1.2 cm<sup>2</sup> Haynes 230 test coupons, one of which they thermally cycled 5 times prior to sending. The non-cycled specimen was used in the tests reported here.

In addition, we also revisited our Phase 2 approach of coating the test articles with Pyromark. We reviewed material from Sandia National Laboratory (SNL) on their new application approach for Pyromark and contacted Sandia about the details of the application process. Our tests were conducted using Haynes 230, both bare and ENi coated surfaces. Surface preparation was done using glass bead media with 60-120 mesh and the paint was applied using a Paasche TG-SET Talon Airbrushing System operating at 35psi. Sandia used ANSI 316L stainless steel, garnet media with 60-120 mesh, and an unspecified model of Binks paint gun. Surface of samples were prepared and chemical cleaning steps were followed. Some samples were not blasted or blasted and then hand sanded with varying grits in order to assess the effect of surface roughness. After the paint was applied the samples were air cured for 18 hours and then moved to the oven. The oven used for the cure cycle is a CM Rapid Temp lab furnace with a 1600°C max continuous run temperature and an atmospheric air environment. Oven temperature and ramp cycles are controlled using a Eurotherm 2404 temperature controller. Oven cure temperature cycle for max operating temperature of ~750°C is as follows:

- i. Heat to 120°C, dwell for 2 hrs
- ii. Heat to 250°C, dwell for 2 hrs
- iii. Heat to 540°C, dwell for 1 hr
- iv. Heat to 700°C, dwell for 1 hr
- v. Cool to 25°C at 5°C/min

The characterization procedure for the coatings is depicted in Figure 34. After the initial cure reflectivity measurements were taken using spectrophotometer (JASCO UV-670). The samples were then cycled and the reflectivity and mechanical robustness

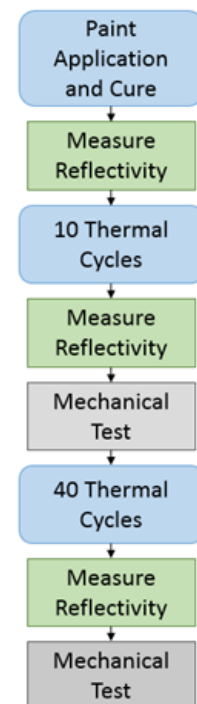


Figure 34. Cyclic test procedure.

was measured. Cycles were completed based on those conducted by Dr. Jin's group. The oven was brought to 750°C as rapidly as possible, in this case it was approximately 8 minutes. The temperature was then held for 15 minutes to ensure complete soak of the coupons. After the soak the temperature was dropped as rapidly as permitted. The cooling time was set to 30 minutes to reach 50°C. Once cooled the cycle automatically repeated.

Reflectivity measurements were taken of each sample after curing and after each set of thermal cycling. Results for each sample are provided in Figures 35(a-c). Fig. 35(d) is a comparison of all three samples after 50 thermal cycles. A plot of the terrestrial solar insolation based on the ASTM G173 data set is provided to determine the greatest contribution section of reflectivity.

Every sample showed signs of increased reflectivity after thermal cycling. The increase in reflectivity was greater between the initial and 10-cycle measurements while the increase in reflectivity was minimal after 40 additional cycles. The black oxide coating from UCSD was very stable and showed very small increases.

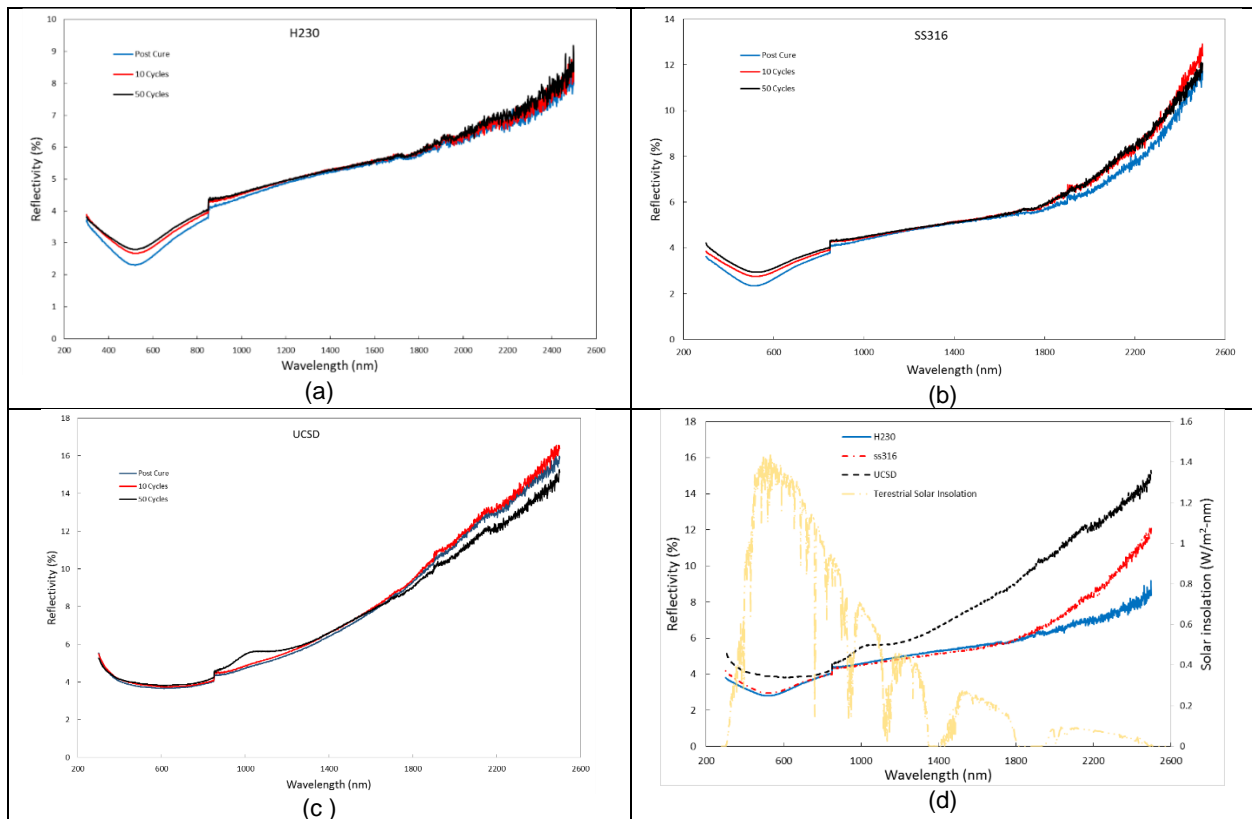


Figure 35. (a) Pyromark 2500 on Haynes 230, reflectivity as a function of wavelength; (b) Pyromark 2500 on SS316, reflectivity as a function of wavelength; (c) UCSD black oxide on Haynes 230, reflectivity as a function of wavelength; (d) reflectivity as a function of wavelength comparison of each sample with the inclusion of solar insolation.

Mechanical testing was performed in accordance with the ASTM D3359-97 standard for adhesion by tape test. Scotch pressure sensitive tape by 3M was utilized. Since the test specimens were small, method B outlined in the standard was followed. An “X” formed by cutting two intersecting lines with a small angle of 30-45 into the coating such

that bare metal shows. The tape was then applied and rubbed into place until uniform coloration occurred. The tape used went from a frosty white to clear under complete contact. For consistency the tape was allowed to rest for 1 minute prior to removal. Pyromark coating showed no signs of peeling except within the cut line giving a rating of 5A, which is satisfactory. The UCSD coating showed signs of peeling well away from the incision and given a rating of 0A. This lifting of the coating did not expose bare metal since the coating is substantially thicker than Pyromark. More detail is required on the coating methods of Dr. Jin's group to fully understand the mechanical properties. From the limited tests conducted, Pyromark is shown to be the superior coating in terms of mechanical performance.

On June 19<sup>th</sup> the power supply for the flux generator failed and has been shipped to the vendor for repair. Due to the failure of the power supply no "on sun" tests have been conducted using the improved curing process of Pyromark 2500. However, based on the spectral values of the reflectance as compared with the spectrum of the Xenon short arc lamp, which is the source of simulated radiation [See Fig. 35(d)] we expect that the Pyromark coated receiver would perform slightly better than the UCSD coating. The wavelength range with the lowest reflectivity in Pyromark coating nearly matched the peak in the arc lamp simulated insolation. We have coated our molten salt test article with Pyromark 2500 and when we test the molten salt test article at 400 W/cm<sup>2</sup> we will get some indicate of the impact of high flux on the Pyromark.

**3.7 Task 8 Commercial Receiver Design (T-8):** The objective of this task is to synthesize the results from the previous seven tasks and develop a conceptual design of a 1 sq. meter micro-channel solar receiver module consisting of multiple unit cells, and a complete commercial scale solar receiver consisting of multiple modules. The receiver will be designed to heat sCO<sub>2</sub> from 550°C to 650°C at a pressure of 200 bars. The receiver will be sized to provide thermal energy to a 100 MW<sub>e</sub> power block.

The proposed commercial receiver is a modular, multiscale design (Fig. 2 and 3, pp. 5-6, above). It consists of multiple ~ 1 m<sup>2</sup> heat transfer modules, which are in turn composed of smaller high-flux microchannel unit cells. General thermal performance and feasibility of the receiver design were determined using a multiscale modeling approach. First, resistance network heat transfer and pressure drop submodels of individual unit cells and modules (*i.e.*, array of unit cells) were developed and used to optimize unit cell and module size. The submodels were then integrated into a full scale commercial receiver model to understand the effect of different receiver geometries and non-uniform incident flux on receiver performance. These models allowed detailed quantification of the efficiency, thermal absorption, heat loss mechanisms, and sCO<sub>2</sub> mass flow rate under a variety of conditions. Finally, a more detailed consideration of the pressure loss in the unit cell header system, implications of incident edge flux due to the square module shape, and the required receiver superstructure design and cost were considered.

The results for the commercial receiver design and analysis are discussed below.

**Unit Cell and Module Model:** A computationally efficient, steady state, network resistance heat transfer model of the unit cell geometry was developed using the *Engineering Equation Solver* (F-Chart Software, 2014) platform. The model accounts for internal and external multi-mode heat transfer effects (Fig. 36), and the sCO<sub>2</sub> frictional pressure loss using appropriate correlations from the literature for thermal and hydraulic resistances. The results of Tasks 6 and 7 are used to specify the unit cell micropin geometry and surface absorptivity used in the model. The other required model inputs were incident solar flux, ambient conditions (wind speed, temperature), inlet sCO<sub>2</sub> temperature, and desired sCO<sub>2</sub> outlet temperature. With these, the model calculates the mass flow rate of the sCO<sub>2</sub> per unit cell, thermal efficiency, unit cell surface temperature, total heat transfer, and pressure drop through the pin array.

To reduce the number of fluid connections, it was desired that each 1 m<sup>2</sup> module contains the fewest number of unit cells possible, while also maintaining the total module pressure drop (pin fin array + header losses) less than 4 bar. Using the unit cell model at the design flux of 110 W/cm<sup>2</sup> and a fixed unit cell width of 100 cm, the unit cell length flow length was incremented until the maximum pin array pressure drop of 3.64 bar (providing a  $\Delta P$  allowance for the header system) was achieved. This resulted in a selected unit cell size of 8 cm × 100 cm (Fig. 37), where a pressure drop less than 3.64 bar and an efficiency ~95% can be achieved. Higher thermally efficient unit cells can be achieved by increasing the unit cell length, however an increase in unit cell length (and overall size) will increase the required mass flow rate of the sCO<sub>2</sub> and therefore increase the pressure drop, yielding an unrealistic pumping requirement.

The thermal efficiency and heat loss modes of the 8 cm × 100 cm unit cell are shown in Figs. 38 and 39, respectively, as a function of incident flux. The efficiency is very

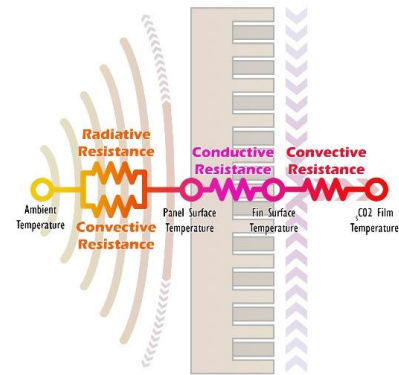


Figure 36: Schematic of Unit Cell Heat Transfer Resistance Network

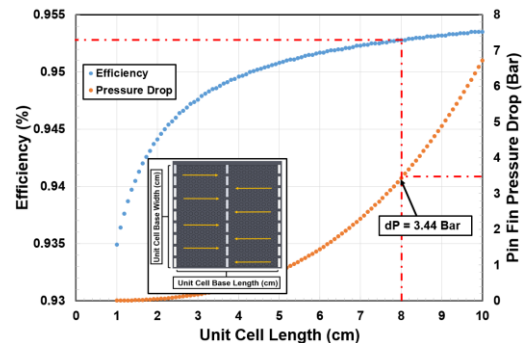


Figure 37 – Unit cell thermal efficiency pressure drop versus unit cell length with width = 100 cm

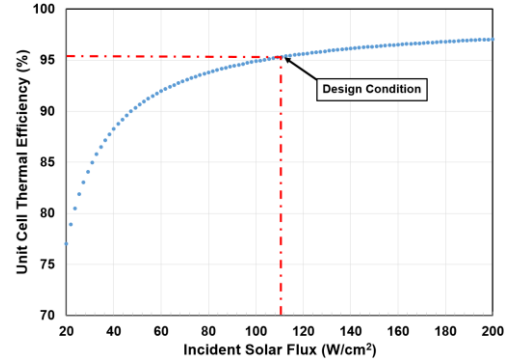


Figure 38. Unit cell thermal efficiency versus incident solar flux.

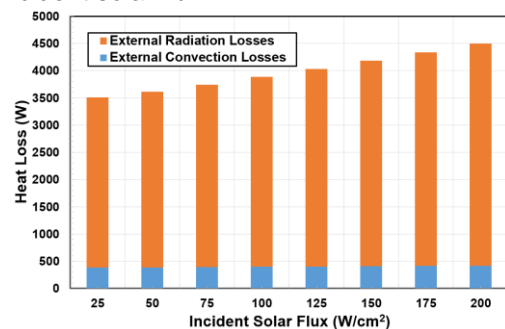


Figure 39. Unit cell convection and radiation losses versus incident solar flux.

sensitive to the incident fluxes at low values ( $\sim 20$  to  $60 \text{ W/cm}^2$ ), however, as the incident flux increases beyond  $100 \text{ W/cm}^2$ , the efficiency begins to approach approximately steady-state with an efficiency between 95% and 98%. As the incident flux on the module increases, the total external heat loss will also increase due to the increase in surface temperature and the associated radiation and convection losses. The relative contribution of convective and radiation losses as a function of incident flux are shown in Figure 39. With an increase in incident surface flux, the convection heat loss is relatively constant while the re-radiation heat loss increases dramatically due to the exponential dependence on surface temperature. At an incident flux of  $200 \text{ W/cm}^2$  the heat loss in the form of re-radiation increases by 35% from an incident flux of  $25 \text{ W/cm}^2$  as compared to a 12.9% increase in convection losses.

**Commercial Receiver Model:** The use of multiple receiver modules allows the shape of a full central receiver to be customized to the flux pattern of a specific heliostat field. To explore this, three different central receiver module configurations were investigated, shown in Figure 40. Each design had the same number of modules (*i.e.*, equivalent surface area) and were 10 modules in height ( $\sim 10 \text{ m}$ ). The baseline design is a cylindrical collector with 25 panels circumferentially. Using a *DELSOL* non-uniform flux distribution developed by [5] as a basis, a scaled non-uniform flux distribution was created for the present study.

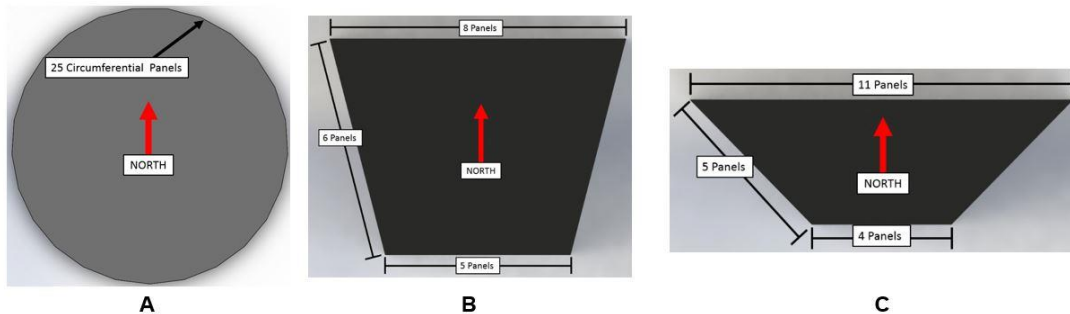


Figure 40. (A) Cylindrical receiver design, (B) modified receiver design # 1, (C) modified receiver design # 2 with 10 modules in height and a total of 250 individual modules.

The flux distribution assumed a 53% drop in incident flux from the northern to southern panels (circumferentially) with a peak flux of  $170 \text{ W/cm}^2$  and an average flux of  $115 \text{ W/cm}^2$ . The vertical change in incident flux was assumed negligible. The important results for the three different designs is shown in Table 4. The baseline cylindrical receiver achieved a heat input to the  $\text{sCO}_2$  of 252.7 MW of thermal energy at an efficiency of 95.5%. By modifying the receiver to increase the north facing surface area (higher local incident flux), an increase in absorbed thermal energy at a higher efficiency can be

Table 4. Comparison of receiver designs

	Baseline Receiver	Receiver # 1	Receiver # 2
Total Receiver Incident Flux	278.6 MW	292.3 MW	304 MW
Total Receiver Heat Input $\text{sCO}_2$	252.7 MW	265.6 MW	276.7 MW
Total Receiver Reflection Losses	13.9 MW	14.6 MW	15.2 MW
Total Receiver Heat Losses	12.0 MW	12.1 MW	12.2 MW
Overall Receiver Efficiency	95.5%	95.6%	95.8%

achieved. The modified receiver design 1 and 2 increased the absorbed thermal energy by 5% and 9.5%, respectively, with an increase of 0.2 and 0.5 efficiency points, respectively. The full receiver model allows the effect of changes in geometry (from the micro-pin unit cell to the layout of the full receiver) on the thermal performance to be understood. The model can be used as a design tool to tailor the global receiver shape to different heliostat fields.

**Header Pressure Loss:** Fluid will be distributed to each unit cell through semi-circular headers (see Fig. 41) attached to the backside of the unit cell. To minimize total module pressure loss and ensure uniform fluid distribution, the pressure loss in the header system should be on the order of 10% of the pressure loss through the pin fin array. As the unit cell width increases, the header flow length and mass flow rate both increase, yielding higher total pressure losses.

A discretized pressure loss model accounting for frictional and minor losses in the header system was developed to ensure a reasonably sized header for the selected unit cell geometry (8 cm x 100 cm). Fig. 42 shows this trend, as well as the calculated minimum header pipe diameter to achieve the targeted header pressure loss. For the selected 8 cm x 100 cm unit cell length, a minimum inner header diameter 2.725 cm is required.

**Side Flux Considerations:** When the square modules are mounted on a full scale central receiver, the surface edge of the module may be subjected to incident flux from the heliostat field, as seen in Figure 43 and Figure 44. To determine the effects of this incident flux, an analysis was conducted on the 8

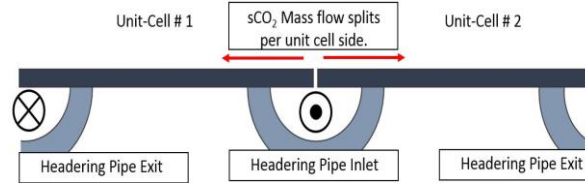


Figure 41. Header design of individual unit cells for flow distribution.

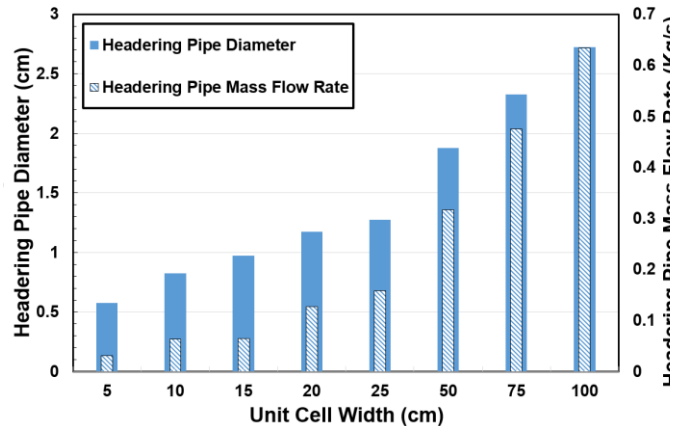


Figure 42. Discretized pressure drop for various unit cell flow length dimensions.

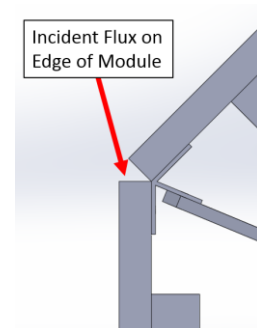


Figure 43. Edge incident flux schematic.

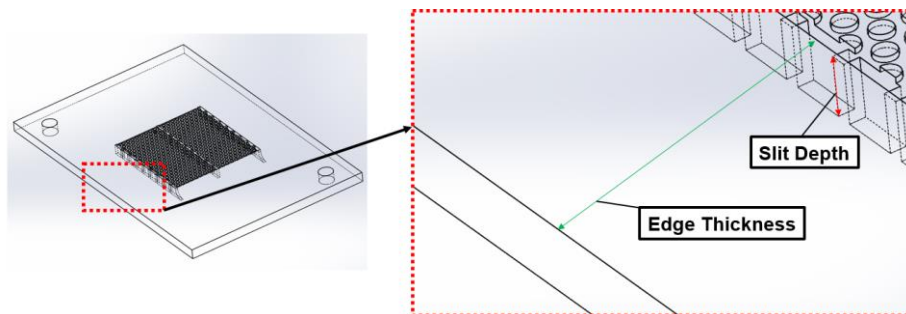


Figure 44. Unit cell edge dimensions.

cm x 100 cm unit cell at the design incident surface flux of 110 W/cm<sup>2</sup>, as seen in Figure 45. It was assumed that the edges will be cooled by the inlet headers, which will have sCO<sub>2</sub> at 550°C. As the edge thickness increases, the edge surface temperature will increase from a nominal value of approximately 600°C to a value of ~1225°C at a thickness of 2 cm due the increased conduction resistance. We anticipate that the edge thickness in a final design will be on the order of a few millimeters resulting in a material temperature of 650°C. The side flux model can be used to understand the thermal and mechanical tradeoffs when specifying the unit cell edge thickness.

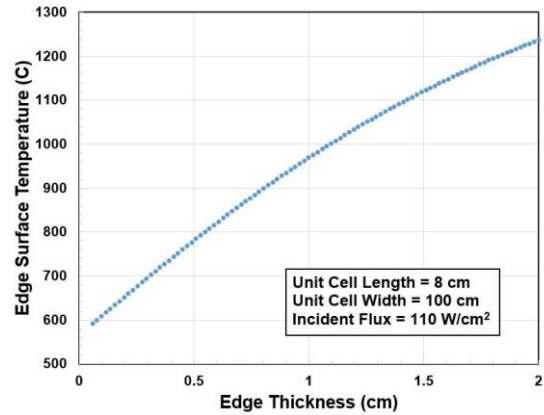


Figure 45. Edge surface temperature versus edge thickness.

**Structural Analysis:** Finally, a structural design and analysis of the receiver was conducted by members of the OSU School of Civil and Construction Engineering. The weight of the individual modules, fluid, piping, and wind loads were considered in the analysis. A 3D rendering of the structure for a cylindrical 250 module receiver can be seen in Figure 46. The structure is a space truss with a central spine connected to outrigger frames that support the modules. The itemized weight and material cost of the structure, piping and receiver modules are provided in Table 5. The material used in this cost estimate is Haynes 230 to prevent thermal failure of the structure due to the high temperature application. It is likely that the entire structure would not experience extreme thermal condition and alternative structural material can be used.

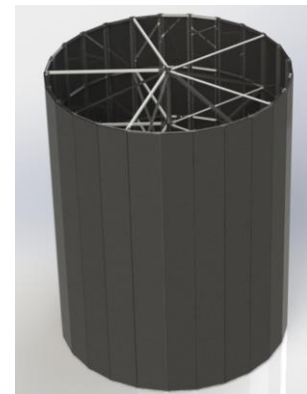


Figure 46. Rendering of commercial receiver with structural components

Table 5. Full scale receiver design estimates

Structural Material	Haynes 230
Structural Weight (Structure Only)	24,300 lbs
Structural Weight (with Modules and Piping)	35,000 lbs
Estimated Structural Costs	\$636,000
Material Cost Per Kilowatt	\$2.54/kW

This task demonstrates the feasibility of using the microscale unit cells in a full scale, 250 MW thermal solar receiver composed of multiple modules. The modular design allows unconventional central receiver geometries that can be tailored to the specific field, as well as having the potential for independent control of the sCO<sub>2</sub> mass flow rate to each module to maintain uniform fluid outlet temperature. The unit cell model showed the potential for rapid parametric evaluation and optimization of different pin fin array geometries, surface absorptivity, unit cell length and width, and operating conditions. The multi-scale full receiver model showed that at the design non-uniform incident flux and surface emissivity, a global receiver thermal efficiency of >90% can be achieved for

the three different configurations considered. With an increase in northern-facing panels, while still keeping the total surface area constant, the absorbed solar thermal energy can be increased while also increasing the receiver efficiency.

The modular receiver design also has advantages for reducing construction and installation costs. Assuming a receiver with 250 panels (~8 m diameter and 10 m tall), the modular design can be shop fabricated with 5 panels sections and 5 structural brace sections and shipped to the field site for pre-assembly (Fig. 47). This would significantly reduce cost compared to build-in-place designs.



Figure 47. Rendering of modular receiver construction.

**4.0 CONCLUSIONS:** Based on the results of this projects we have the following conclusions.

The Project Has Successfully Demonstrated the Lab-Scale Technical Feasibility of the MSR and Achieved Most of the Project Milestones and Go/NoGo Decision Points –  
Specific technical conclusions include:

- **Suitable Material and Fabrication Options Exist** – While further research is necessary to identify the optimum combination of nickel superalloys and fabrication techniques, we have identified one combination (Haynes 230 with sinker EDM and diffusion bonding) as a viable fabrication approach capable of producing test articles able to operate at HTF temperatures up to 650°C and pressures up to 125 bars. Additional research is required to ensure that we have a material and fabrication approach suitable for higher HTF temperatures and are able to operate for at least 10,000 thermal cycles. These accomplishments meet milestones **M4.1, M4.2, Phase 1 G/NG-2** and **Phase 2 G/NG-1**.
- **sCO<sub>2</sub> Results** – Simulation and testing of the sCO<sub>2</sub> separate effects and integrated test articles confirm our ability to operate the devices with incident solar fluxes up to 100 W/cm<sup>2</sup> while heating sCO<sub>2</sub> to 650°C at a pressure of 120 to 200 bars while having thermal losses on the order of 5% for an overall receiver efficiency of 90% (assuming a receiver absorptivity of 95%). These accomplishments meet milestones **M1.1, M2.1, M3.1, M5.1, M5.3, Phase 1 G/NG-1, Phase 1 G/NG-3** and **Phase 2 G/NG-2**. This is a radical improvement over other published solar receiver designs for gaseous HTRs, resulting in a receiver which is significantly smaller, less expensive, and more efficient than other published solar receivers for gaseous HTFs. The development of the integrated test article with multiple unit cells and a distribution system is still in progress. As described above, our original test article was not successfully bonded and we redesigned the device. The new device has been patterned using sinker EDM and as of July 15<sup>th</sup> the test article is at the diffusion bonding contractor for bonding. We expect to receive and pressure test this device at 200 bars before the final presentation on July 28<sup>th</sup>. If we are successful this will meet milestones **M6.1** and **M6.2**.
- **Molten Salt Results** – Simulation results have indicated that the molten salt test

article can operate with an incident flux of 400 W/cm<sup>2</sup> and a molten salt exit temperature of 600°C while having thermal losses on the order of 1% of the absorbed flux, meeting milestones **M1.2**. We have encountered significant experimental challenges in working with molten salt including corrosion of the reflector in our flux generator requiring the replacement of the reflector and the failure of our power supply. We have experimental results at fluxes up to 150 W/cm<sup>2</sup> which are consistent with the simulation results (when adjusted for surface optical properties and flux). We are currently having the power supply repaired and hope to be able to test at 400 W/cm<sup>2</sup> in the next few weeks, meeting milestone **M5.2**.

- **Optical Coatings** – The results of our investigation of high temperature high absorptivity optical coating are encouraging. Both the UCSD coating and Pyromark applied using the SNL application method have attractive optical properties after thermal cycling. However, mechanical testing (Tap test) indicated that Pyromark was more a more robust coating. While this is only a preliminary investigation and more testing is required to qualify these coatings for commercial application the results suggest that a high temperature high absorptivity optical coatings are feasible. Based on what we know now, we would select Pyromark applied using the SNL application approach. These results meet milestone **M7.1**. UCSD was unable to coat one of our sCO<sub>2</sub> test articles, allowing a test of the coating under high flux conditions but we have coated our molten salt test article with Pyromark and we will be able to observe the impact of high fluxes (up to 400 W/cm<sup>2</sup>) on the coating when we test the molten salt test article at these high fluxes. These results will meet **M7.2**.
- **Commercial Design** – Our conceptual design of a commercial scale solar receiver identified potential solutions to a number of design issues associated a receiver fabricated from a large number of individual 1 m<sup>2</sup> receiver panels. We did not find any issues that could not be addressed by straightforward design features or any problems that threatened the technical viability of the concept. These results meet milestone **M8.1**.

The Project Has Successfully Demonstrated the Value of the MSR to Solar Central Receiver Power Generation – The results of this study have demonstrated the value of the MSR. The MSR's ability to operate at high temperature with high efficiency (not requiring a cavity receiver design) allows the use of advanced HTF's and more efficient high temperature power cycles. This is true for both gaseous and liquid HTF's. In addition, the small size of the receiver appears to result in a significant reduction in the cost of the receiver and has the potential to significantly exceed the Sunshot cost goals for the receiver and tower.

The Project Has Successfully Opened New Design Space for System Designers. We Do Not Fully Understand the Overall Impact of the MSR on Improving Plant Performance and Cost - While the incident flux of 100 W/cm<sup>2</sup> for sCO<sub>2</sub> receiver designs is well within the capability of current concentrator field designs the ability of the MSR to operate at 400 w/cm<sup>2</sup> flux with molten salt and perhaps 800 w/cm<sup>2</sup> flux with liquid metals opens up new design space for solar power plant designer enabling the efficient operation of the receiver at very high temperature with an extremely compact and possibly

low cost receiver. This may require the redesign of the concentrator field with smaller heliostats. With a number of new heat transfer fluids being developed, we need a detailed system study to identify what combination of advanced CSP technologies will allow the MSR to make its greatest contribution to reaching the Sunshot cost goals for concentrating solar power.

**5.0 BUDGET AND SCHEDULE:** Spending is summarized on the table below. This is not our final spending summary because several expenses have not yet reflected in the spending summaries. In addition, one of our cofunding accounts will be active until the end of July.

Recipient:		OSU-DROST		
DOE Award #:		DE-EE0005801		
<b>Spending Summary for SF 424A Budget Forms</b>				
Object Class Categories	APPROVED BUDGET	TOTAL SPENT TO DATE	Forecasted Spending (FINAL COSTING FOR FY14 SCOPE)	
a. Personnel	\$295,435	\$283,720	\$295,000	
b. Fringe Benefits	\$62,865	\$64,341	\$64,341	
c. Travel	\$14,000	\$9,320	\$12,500	
d. Equipment	\$20,000	\$28,187	\$28,187	
e. Supplies	\$86,778	\$92,995	\$95,995	
f. Contractual	\$20,000	\$9,510	\$9,510	
g. Construction	\$0	\$0	\$0	
h. Other	\$122,369	\$113,954	\$118,804	
<b>i. Total Direct Charges (sum of a to h)</b>	<b>\$621,447</b>	<b>\$602,027</b>	<b>\$624,337</b>	
j. Indirect Charges	\$219,790	\$204,790	\$216,900	
<b>k. Totals (sum of i and j)</b>	<b>\$841,237</b>	<b>\$806,817</b>	<b>\$841,237</b>	
DOE Share	\$841,237	\$806,817	\$841,237	
Cost Share	\$183,588	\$171,588	\$183,588	
<b>Calculated Cost Share Percentage</b>	<b>21.8%</b>	<b>21.3%</b>	<b>21.8%</b>	

Relative to our schedule, the first phase of the project lasted from August 1<sup>st</sup> 2012-August 31<sup>st</sup> 2013. The second phase of the project lasted from September 1<sup>st</sup> 2013 to August 31<sup>st</sup> 2014 while the third phase lasted from November 1 2014 to June 30<sup>th</sup> 2015. A one month no cost extension was requested for Phase 3 to allow the fabrication of a second round of integrated test articles.

**6.0 PATH FORWARD:** Based on the encouraging results of this project we have initiated a number of follow-on activities and plan to initiate several more. Follow on activities are to a great extent determined by the technology readiness of the concept (TRL 3). On-going activities include:

1. Preparation of a follow-on proposal to the Sunshot Apollo solicitation focused on moving the MSR from lab scale test article (TRL-3) to commercial scale receiver panel tested on sun at Sandia National Laboratory (TRL-5).
2. Formation of a commercialization team that consists of the Oregon Nanoscience and Microtechnology Institute (ONAMI), Oregon Built Environment and Sustainable Technology Institute (OregonBEST), ECOKAP, and Orion Ventures to advance the commercialization of the MSR.
3. Conducting related funded research on similar sCO<sub>2</sub> heat exchangers and production cost estimates for the MSR.
4. Assembled a team consisting of OSU, PNNL and the National Energy Technology Laboratory (NETL) which is pursuing research funding for a related combustion technology that using the MSR concept and high flux catalytic combustion allowing the use of gaseous fossil fuels as a heat source for sCO<sub>2</sub>.
5. Development of an invention disclosure on the concept.

## 7.0 REFERENCES:

1. Fletcher, E.A., 2011 Solar Thermal Processing: A Review, "ASME Journal of Solar Energy Engineering, Vol. 123 pp.63-74.
2. U.S. Department of Energy, "SunShot Vision Study," *Paper No. DOE/GO-102012-3037*, 293pp., 2012.
3. Romero, M, R. Buck, and J.E. Pacheco, "An Update on Solar Central Receiver Systems, Projects, and Technologies," *J Sol Energ*, Vol. 124, pp. 98-108, 2002.
4. Pacheco, J.E., "Final Test and Evaluation Results from Solar Two Project," *Paper No. SAND2002-0120*, Sandia National Laboratory, PO Box 5800, Albuquerque, NM, 2002.
5. Kolb,G.J., "An Evaluation of the Next Generation of High Temperature Molten Salt Power Towers," *Paper No. SAND11-9320*, Sandia National Laboratory, PO Box 5800, Albuquerque, NM, 2011.
6. Kolb,G.J., C.K. Ho, T.R. Mancini, and J.A. Gary, "Power Tower Technology Road Map and Cost Reduction Plan," *Paper No. SAND11-2419*, Sandia National Laboratory, PO Box 5800, Albuquerque, NM. 2011.
7. U.S. Department of Energy, "High Efficiency Receivers for Supercritical Carbon Dioxide Cycles," *Paper No. DOE/GO-102012-3661*, SunShot Concentrating Solar Power Project Description. [www.solar.energy.gov/sunshot/csp\\_sunshotrnd\\_brayton.html](http://www.solar.energy.gov/sunshot/csp_sunshotrnd_brayton.html).
8. Klein, S.A., 2014 "F-Chart Software:EES".